Bulletin of the Seismological Society of America, Vol. 95, No. 6, pp. 2232–2258, December 2005, doi: 10.1785/0120020106

3D Cohesive End-Zone Model for Source Scaling of Strike-Slip Interplate Earthquakes

by Scott J. Wilkins* and Richard A. Schultz

Abstract A 3D, static fracture mechanics model of earthquake rupture that incorporates cohesive end zones (CEZs), or zones of increased frictional strength, is tested to determine whether it helps to understand the observed scaling behavior of average slip with rupture dimensions for shallow (<20 km), continental, interplate strike-slip earthquakes. Our new compilation of average source parameters suggests that (1) average slip increases with aspect ratio (along-strike length/down-dip width), although in decreasing proportions for progressively larger aspect ratio ruptures, and (2) a gradual scaling change exists at an aspect ratio of ~6. These general trends match the functional form predicted by the CEZ model. Despite these general trends, significant scatter in average slip is apparent among similarly sized ruptures. We test the hypothesis that the CEZs represent strength heterogeneities along the rupture surface that result from velocity-strengthening frictional behavior; and that this heterogeneity in frictional behavior along the fault is the primary reason for the failure of a universal (constant stress drop) scaling law. CEZ lengths are measured from slip and stress drop distributions determined from published inversions of geophysical data for the 1984 Morgan Hill, 1992 Landers, 1999 Hector Mine, and 1999 İzmit earthquakes, and range from ~15 to 40% of the rupture segment lengths. These lengths are an order of magnitude larger than that inferred from characteristics of high-frequency seismic radiation (i.e., f_{max}). These data indicate that the ratio of average coseismic slip to rupture length decreases in the presence of large CEZs. Measured CEZ lengths, rupture dimensions, and average slip are used to calculate average resolved shear-driving stresses and CEZ shear-yield strengths on the order of ~10–30 MPa. In our new model of earthquake rupture, stress drop is predicted to be a small fraction of fault strength and thus supports a partial stress drop model of earthquake rupture for strike-slip interplate events.

Introduction

The scaling behavior of earthquake source parameters has received considerable attention because of its implications for seismic hazards (e.g., Wells and Coppersmith, 1994) and the potential to provide insight regarding the physics of earthquakes (e.g., Kanamori and Anderson, 1975). The relationship between slip and rupture dimensions for continental strike-slip earthquakes is especially important for both reasons but has been difficult to establish. Various researchers have reached different conclusions on the subject, partly because of the lack of large strike-slip earthquakes (e.g., Scholz, 1982, 1994a,b; Romanowicz, 1992, 1994; Bodin and Brune, 1996; Yin and Rodgers, 1996; Mai and Beroza, 2000; Shaw and Scholz, 2001; Miller, 2002a,b).

The central issue concerns whether average slip (u_{avg}) is proportional to rupture length (l) for continental strike-slip earthquakes of all sizes, or if this scaling behavior differs for large ruptures that have rupture lengths greater than the seismogenic thickness (w, i.e., $l > w$). If strike-slip earthquakes were to exhibit scale-dependent behavior, with average slip proportional to rupture length (Scholz, 1982), stronger ground motions (e.g., peak acceleration) would be predicted for ruptures with longer lengths (e.g., Lee *et al.*, 2000). In contrast, if strike-slip earthquakes exhibit scale-independent behavior, as would be the case when average slip remains constant regardless of rupture length, similar ground motions would be predicted for a wide range of rupture lengths. In this article we propose that a more complex scenario may also exist, where average slip is only partly dependent on

*Present address: Structure, Traps, and Seals Team, Shell International Exploration & Production Inc., Bellaire Technology Center, P.O. Box 481, Houston, Texas 77001-0481. Scott.Wilkins@Shell.com

the rupture length, and other factors such as frictional strength influence the magnitude of slip.

Researchers have previously suggested that the width of the seismogenic zone (w), which commonly ranges from ~10 to 20 km within continental crust (e.g., Marone and Scholz, 1988; Maggi *et al.*, 2000), should exert an important mechanical influence on earthquake slip behavior (Knopoff, 1958; Kanamori and Anderson, 1975; Scholz, 1982). Under the assumption that earthquakes behave as cracks in an elastic medium, elastic models have been used to suggest that average slip (u_{avg}) should scale with rupture radius (r) for small ruptures, where $l = w$ and is less than the seismogenic thickness, and with rupture width (w) for large ruptures with lengths (l) greater than w (Eshelby, 1957; Knopoff, 1958; Kanamori and Anderson, 1975). Consequently, a change in the scaling behavior between u_{avg} and l is expected to occur once observed rupture lengths are on the order of the width of the seismogenic zone (~10–20 km). This particular model has been referred to as the "W model" because average slip during large events should be related to rupture width (Scholz, 1982). In contrast to this model, Scholz (1982) concluded that the ratio of u_{avg} to l is approximately constant for all observed strike-slip ruptures, regardless of rupture length, and referred to this relationship as the L model.

Upon re-examination of updated data, subsequent researchers suggested that a scaling change does occur and concluded that it is more consistent with a W model (Romanowitz, 1992; Mai and Beroza, 2000; Shaw and Scholz, 2001). However, the change in scaling behavior has been observed at rupture lengths much greater than the seismogenic thickness and remains problematic because no physical feature correlates with this length scale. The change in scaling behavior has been proposed to occur at $l = 200$ km according to Scholz (1994b), at $l = 60$–70 km according to Romanowicz (1992), and at $l/w > 10$ according to Shaw and Scholz (2001). Various mechanical models (Bodin and Brune, 1996; Yin and Rogers, 1996) indicate that this crossover length depends on rupture width (~75 km rupture length for a width of 15 km). Yin and Rogers (1996), Mai and Beroza (2000), and Shaw and Scholz (2001) observed that, for strike-slip events with coseismic rupture lengths much greater than the seismogenic thickness ($l \gg w$), average slip continuously increases for increasingly larger rupture lengths, but at reduced rates compared with events with $l < w$. Both of these observations, the large crossover lengths at which scaling changes are interpreted to occur and the reduced-rate increase in slip for large-aspect ratio (l/w, where $l \gg w$) ruptures are difficult to reconcile with earlier elastic models (Mai and Beroza, 2000).

One clear observation is that the earthquakes with similar rupture dimensions often have a significant difference in average slip and thus require a variation in stress drop (Bodin and Brune, 1996; Yin and Rogers, 1996; and Mai and Beroza, 2000; Shaw and Scholz, 2001; Miller, 2002b). However, the physical mechanism responsible for this variation in stress drop is unclear. Miller (2002b) suggested that variations in pore pressure are a possible mechanism for modulating the frictional strength and, thus, stress drop. In contrast, numerical modeling results of Shaw and Scholz (2001) have been interpreted to suggest that the scatter in the slip–rupture dimension relationship is attributable to variations in initial strength conditions along the fault (also see discussions in Bodin and Brune [1996] and Mai and Beroza [2000]), which arise from variations in previous slip magnitudes associated with a spatially heterogeneous rupture history.

In this article, we examine whether a (3D) fracture mechanics model of fault slip (Schultz and Fossen, 2002; hereafter referred to as S&F) supports the hypothesis that strength heterogeneities are responsible for differences in stress drop among similarly sized ruptures. We do so by testing the S&F model against an updated compilation of source parameters and interpreted cohesive end-zone (CEZ) sizes measured from distributions of slip and stress drop associated with strike-slip earthquakes. Over 90% of the earthquakes we analyze have rupture widths >10 km, which indicates that we are investigating the scaling behavior of large earthquakes that span the seismogenic thickness. In contrast to the earlier elastic models that incorporated either rupture length or width in their analyses (Eshelby, 1957; Knopoff, 1958), the S&F 3D model incorporates both dimensions and is thus more similar to recent models (Bodin and Brune, 1996; Yin and Rogers, 1996; Shaw and Scholz, 2001; Miller, 2002a,b). The fundamental difference between the S&F and previous models is that it explicitly includes a CEZ, manifest as a region where slip and slip gradients dramatically decrease from larger values characteristic of the central (or yielded) portion of the rupture (e.g., Dugdale, 1960; Barenblatt, 1962; Palmer and Rice, 1973; Rudnicki, 1980; Cowie and Scholz, 1992).

We measure CEZ dimensions from distributions of slip and stress drop that are produced by inverting some combination of strong-motion records, teleseismic body waves, mapped surface offsets, Global Positioning System (GPS) displacement vectors, and Interferometric Synthetic Aperature Radar (InSAR) data (e.g., Beroza and Spudich, 1988; Beroza and Mikumo, 1996; Wald and Heaton, 1994; Peyrat *et al.*, 2001; Delouis *et al.*, 2002; Ji *et al.*, 2002). Measured CEZ sizes for four well-studied earthquakes provide support for the S&F model in that differences in CEZ lengths directly correlate with differences in stress drop, or the ratio of average slip to rupture length, and thus seem responsible for the scatter observed in the scaling behavior of strike-slip source parameters. Similar to previous models (Yin and Rogers, 1996; Mai and Beroza, 2000; Shaw and Scholz, 2001; Miller, 2002a,b), the S&F model also suggests that average slip is a general function of fault length, although slip increases at lower rates for ruptures with large aspect ratios compared with ruptures with smaller aspect ratios.

On the Applicability of CEZ Models to Earthquakes

A CEZ is a mathematical approximation used in mechanical models of faulting and fracturing to avoid the unphysical singularity (i.e., infinite magnitude) in stress that develops at a fault tip in models that assume linear elastic fracture mechanics (LEFM) (e.g., Ingraffea, 1987; Lawn, 1993). The CEZ is represented by cohesive or frictional forces near the fault tip, which act to oppose the applied load that drives fault slip. This reduces the magnitude of stress at the fault tip to physically reasonable values that are on the order of the yield shear strength of the material (e.g., healed fault surfaces or intact rock). Cohesive forces are assumed to arise from microstructural inelastic processes, such as the nucleation and growth of distributed fracture arrays in a process zone (e.g., Ingraffea, 1987; Vermilye and Scholz, 1998). This zone has also been referred to as a frictional breakdown zone (Cowie and Scholz, 1992), where the frictional resistance to slippage is greater near the fault tip relative to the localized slip surface (Okubo and Dieterich, 1984; Martel and Pollard, 1989; Cowie and Scholz, 1992). The fundamental physical manifestation of CEZs is a region where slip and slip gradients dramatically decrease from larger values characteristic of the central (or yielded) portion of the rupture (region 2*c* in Fig. 1) and taper toward zero at the rupture tip or segment boundaries (region *s* in Fig. 1; Cowie and Scholz, 1992; Rubin, 1993; Bürgmann *et al.*, 1994; Cooke, 1997; Martel, 1997; S&F). Slip gradients near the rupture tip are smaller for CEZ models than for LEFM models. LEFM slip distributions exhibit elliptical slip distributions and maximum slip gradients at the rupture tip, which induce a near-tip-stress singularity (Fig. 1) (Cowie and Scholz, 1992; Rubin, 1993; Bürgmann *et al.*, 1994).

CEZs are modeled by invoking a region of increased frictional strength (τ_y for a resolved shear stress only) (Fig. 1) near the rupture edge (Rudnicki, 1980; Cowie and Scholz, 1992; Bürgmann *et al.*, 1994; S&F). Within the CEZ, friction decreases from the highest values at the fault tip where displacement is zero, to the lowest values at the CEZ tail, where displacement increases to u_{cez} (Fig. 1). Friction in the CEZ decreases from values assumed to be associated with healed fault rock (Cowie and Shipton, 1998) or fractured rock that has not yet localized into a well-developed sliding surface (Cowie and Scholz, 1992; Cooke, 1997), to the residual frictional strength (τ_f) of the well-developed, localized fault surface that repeatedly hosts larger magnitudes of slip during rupture (2*c*; Fig. 1). Increased frictional resistance in the CEZ has been associated with the lack of wear (e.g., Cooke, 1997) relative to the central portion of the fault, and the lack of wear is commonly associated with reduced displacements (e.g., Scholz, 1990, pp. 66–73, 110–115). Fault rocks that have not experienced significant wear commonly exhibit distinctive characteristics relative to those that have (Cooke, 1997), such as (1) increased roughness of the fault (Byerlee, 1967), (2) decreased thickness of fault gouge (Biegel and Sammis, 1989), (3) increased grain size of the gouge (Gu and Wong, 1994), and (4) the lack of gouge consolidation (Marone and Scholz, 1988; Marone *et al.*, 1990). Portions of a fault with these properties are likely to experience velocity-strengthening frictional behavior and are associated with regions that experience negative stress drops during laboratory experiments (see reviews by Marone [1998] and Scholz [1998]).

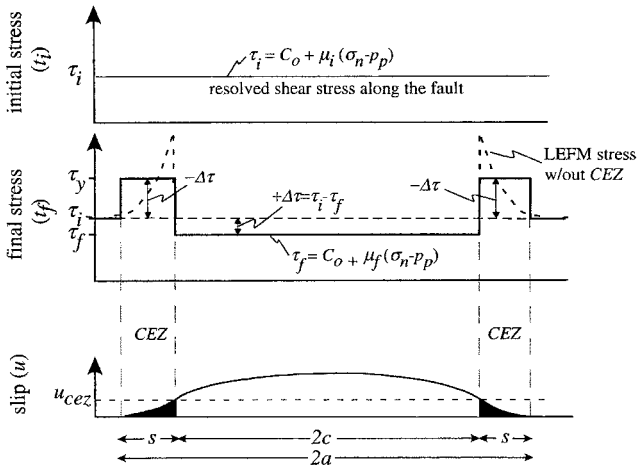

Figure 1. Schematic distribution of stress conditions (resolved along the rupture surface) and slip for an elastic rupture with cohesive end zones (CEZs). Driving stress (τ_d) represents the resolved shear stress along the fault before slip (τ_i) that is reduced to residual frictional strength after the slip event (τ_f). Peak strength (τ_y) represents the increased frictional strength of the CEZ. Stress drop is negative in the CEZ ($\tau_i - \tau_y$) and positive elsewhere ($\tau_i - \tau_f = [\mu_i - \mu_f] * [\sigma_n - p_p]$). Notice the inflection in the displacement profile at u_{cez}, marking the beginning of the CEZ (s), and the near-tip stress singularity that exists without a CEZ (LEFM conditions).

Velocity strengthening of a sliding surface occurs when the base value of friction increases to higher values with an increase in slip rate. This results in a negative stress drop ($-\Delta\tau$; Fig. 1) and indicates that sliding was accommodated in a stable manner, via steady-state creep (e.g., Marone and Scholz, 1988; Marone, 1998; Scholz, 1998). Velocity strengthening also occurs at the brittle-plastic transition, in response to an increase in temperature with depth (e.g., Marone and Scholz, 1988; Blanpied *et al.*, 1995). In contrast, velocity weakening occurs during unstable, seismic (stick-) slip, where the base value of friction (before slippage) is reduced to lower values after an increase in slip rate, and results in a positive stress drop ($+\Delta\tau$; Fig. 1). Slip pulses (Heaton, 1990) that propagate toward a portion of the fault that exhibits velocity-strengthening behavior will be inhibited from propagating farther (Scholz, 1998), although slip may still occur in this zone as the energy from the propagating rupture pulse is dissipated. Velocity-dependent frictional behavior thus presents a mechanism to form CEZs along a pre-existing fault, rendering the CEZ model of fault-

ing applicable to earthquakes that repeatedly rupture the same fault surface.

Because velocity-strengthening regions act to inhibit the propagation of an approaching slip pulse (Scholz, 1998), regions that experience negative stress drops should also produce high frequencies of seismic radiation because high frequencies are commonly generated from rupture-stopping areas or regions of the fault with large gradients in slip (e.g., Zeng *et al.*, 1993). Consequently, researchers have estimated CEZ lengths from f_{max}, the maximum frequency of seismic radiation (e.g., Papageorgiou and Aki, 1983a,b). A comparison between CEZ lengths that we determine from average source parameters and previous estimates from f_{max} is discussed later in this article.

Recognition of shallow-slip gradients on slip distributions determined from surface offsets (e.g., 1999 Hector Mine, California [Scientists from the U.S. Geological Survey (USGS), Southern California Earthquake Center (SCEC), and California Division of Mines and Geology (CDMG), 2000]; 1992 Landers, California [Sieh *et al.*, 1993]; 2001 Kunlun, Tibet [Lin *et al.*, 2002] earthquakes) and calculated from inversions of geophysical data (e.g., 1999 İzmit, Turkey [Delouis *et al.*, 2002]; 1999 Hector Mine, California [Ji *et al.*, 2002]; 1992 Landers, California [Wald and Heaton, 1994; Peyrat *et al.*, 2001]; and 1984 Morgan Hill, California [Beroza and Spudich, 1988; Beroza and Mikumo, 1996]), provide compelling evidence for the existence of CEZs along earthquake ruptures. Furthermore, inversions of geophysical data indicate that these (displacement-defined) regions also exhibit negative stress drops (see below), indicating that these CEZs exhibit velocity-strengthening frictional behavior.

We therefore favor the suggestion that velocity-strengthening frictional behavior, which occurs in a variety of different materials (e.g., unconsolidated gouge) and conditions (e.g., increased temperature or ratio of shear/normal stress change), is responsible for the formation of a CEZ at the perimeter of, or even within, an earthquake rupture patch. This implies that a variety of processes may simultaneously operate to form a CEZ, and furthermore, that CEZs may be semipermanent features that provide a mechanism for the occurrence of characteristic earthquakes.

3D CEZ Model for Fault Slip

The details of CEZ mechanics that were first developed for applications to opening-mode fractures (Dugdale, 1960; Barenblatt, 1962; Rubin, 1993), have also been described with applications to faults (Palmer and Rice, 1973; Rudnicki, 1980; Martel and Pollard, 1989; Cowie and Scholz, 1992; Bürgmann *et al.*, 1994; Cooke, 1997; Li, 1987; Martel, 1997), but most often only in 2D (plane strain) analyses. Although Willemse (1997) used a 3D CEZ model to investigate effects of CEZs on mechanical interaction along segmented arrays of normal faults, and Martel and Boger (1998) investigated the effects of a 3D CEZ on patterns of secondary faulting near fault tips, these 3D models were restricted to circular faults with a circular CEZ surrounding the fault perimeter. S&F derived a general 3D analytical solution for elliptical faults, of which circular faults are an end-member solution. Furthermore, unlike previous fault models that invoke a constant CEZ length relative to the fault radius, the S&F model allows the length of the CEZ to vary, as in work by Chell (1977). Consequently, it is now possible to compare CEZ models of faulting with the wide variety of observed earthquake rupture dimensions and variable CEZ lengths, which we demonstrate are both important parameters required to match observations from strike-slip earthquakes.

Schultz and Fossen (2002) derived an analytical solution for maximum slip along an elliptical fracture with a CEZ from a combination of elasticity theory and postyield elastic-plastic fracture mechanics. The solution is found by modifying the linear elastic relationship between displacements and driving stress, rheology, and fracture dimensions so that the near-tip elastic stress singularities are balanced (i.e., reduced) by invoking a zone of cohesive forces near the rupture tips (i.e., end zone) that resists the driving stress. An elliptical fault is used as an approximation to rupture shapes that are undoubtedly more complex in nature, and it has 21.5% less area than a rectangular rupture with the same length and width. If earthquake ruptures are rectangular, the S&F (elliptical) model would require slightly longer CEZ lengths and smaller stress drops. We refer the readers to Schultz and Fossen (2002) for the full derivation of the 3D CEZ model and introduce the most important equations in the following.

The solution for maximum slip (u_{max}) on a 3D, elliptical fracture with a CEZ is

$$u_{max} = \left[\frac{2(1-\nu)}{G}\right] \cdot \left\{\frac{\tau_d - \tau_y\left[1 - \cos\left(\frac{\pi\tau_d}{2\tau_y}\right)\right]}{\sqrt{\cos^2\theta + \left(\frac{b}{a}\right)^2 \sin^2\theta}\sqrt{1 + 1.464\left(\frac{a}{b}\right)^{1.65}}}\right\} \cdot \left(b\sqrt{\sin^2\theta + \left(\frac{a}{b}\right)^2\cos^2\theta}\right), \quad (1)$$

where τ_d is the driving shear stress, τ_y is the yield shear strength of the CEZ, a and b are the semimajor and semiminor axes of the rupture patch, θ is the angle relative to the semimajor elliptical axis (i.e., angle between the strike [horizontal = 0°] and the dip [vertical = 90°] of the fault plane; see figures 7 and 11 of S&F), ν is Poisson's ratio, and G is shear modulus or rigidity (Fig. 1; equation 11 in S&F). For a strike-slip rupture, $2a$ is the rupture length (l) and $2b$ is the down-dip, cross-sectional rupture height (h, where $h = w$ for a large, vertical strike-slip fault that spans the

seismogenic thickness). The driving stress (τ_d) represents the difference between the remote shear stress resolved along the fault before slippage and after ($\tau_i - \tau_f = [\mu_i - \mu_f] * [\sigma_n - p_p]$; Fig. 1; see Pollard and Segall [1987], p. 290, Cooke [1997], and Martel and Pollard [1989]), where σ_n is normal stress, p_p is pore pressure, and μ_i *and* μ_f are initial (base or static) and final (residual or dynamic) friction, respectively. In models where residual friction is zero (such as this), the driving stress is equivalent to the initial resolved shear stress. All solutions presented in this article incorporate $G = 33$ GPa and $\nu = 0.25$. Equation (1) assumes linear elasticity everywhere in the medium surrounding the fault except near the fault tip, and it reduces to the LEFM solution (Pollard and Segall, 1987) in the presence of strong, negligibly small end zones (by increasing τ_y/τ_d; Cowie and Scholz, 1992; S&F). The half-length of the CEZ (s; Fig. 1),

$$s = \left[\frac{1 - \cos\left(\frac{\pi\tau_d}{2\tau_y}\right)}{\sqrt{1 + 1.464\left(\frac{a}{b}\right)^{1.65}}} \right] \cdot b\sqrt{\sin^2\theta + \left(\frac{a}{b}\right)^2 \cos^2\theta} \quad (2)$$

depends on the angle (θ) relative to the semimajor elliptical axis ($2a$) and is explicitly related to the ratio of driving shear stress to end-zone yield shear strength (τ_d/τ_y) for a given elliptical rupture shape (a/b; S&F). The first term is related to the effective driving stress (see equation 3 below and equations 7b and 10 in S&F) and the second term represents the rupture radius, as a function of θ (S&F). For a strike-slip fault that is longer than it is tall (i.e., $l > w$), calculations of CEZ length along the rupture length (a) direction requires an angle (θ) of 0°, whereas 90° represents the down-dip direction (b, see figures 1 and 7 in S&F). In cases for ruptures with multiple CEZs, s represents half of the total CEZ length observed in the dimension of interest. For a given rupture radius (r), the magnitude of slip at the tail of the CEZ (u_{cez}; Fig. 1) is simply equation (1) $\times$ ($\sqrt{[r^2 - (r - s)^2]}/r$) (e.g., Pollard and Segall, 1987; Bürgmann *et al.*, 1994), where r is represented by the final term in equations (1) and (2) (equation 5 in S&F).

Stress drop varies spatially along the rupture (here as a step function) (Fig. 1) from $\tau_i - \tau_y$ over s to $\tau_i - \tau_f$ over c, where τ_f is the final shear stress after the slip event ($\tau_f = c_o + \mu_F[\sigma_i - p_p]$; i.e., residual frictional strength, Fig. 1). A combination of these two parameters must be considered to calculate an effective stress drop ($\Delta\tau^*$) over the entire fault length ($2a$ or $2b$),

$$\Delta\tau^* = \frac{\tau_d - \tau_y\left[1 - \cos\left(\frac{\pi\tau_d}{2\tau_y}\right)\right]}{\sqrt{1 + 1.464\left(\frac{a}{b}\right)^{1.65}} * \sqrt{\cos^2\theta + \left(\frac{b}{a}\right)^2 \sin^2\theta}} \quad (3)$$

which is equation 9 from S&F. Effective stress drop ($\Delta\tau^*$) magnitudes explicitly include negative stress drops in the CEZ ($\tau_d - \tau_y$) and positive stress drops along the yielded portion of the fracture that corresponds to the difference in initial and residual fault friction.

Effective stress drop magnitudes in the CEZ models are less than stress drops associated with LEFM models because of the cohesive and frictional forces that act along s (see figure 8 in S&F) and are a small percentage ($<\sim 10\%$) of τ_y. This small stress drop relative to shear strength is also similar to that found in laboratory experiments (e.g., Scholz, 1990, p. 91). Equation (3) is more complex than the well-known elastic solution for the uniform, static stress drop along a shear rupture,

$$\Delta\sigma = CG(u_{avg}/r), \quad (4)$$

where r is the smallest dimension of the rupture surface, u_{avg} is average slip per event, G is shear modulus, and C is a nondimensional constant that accounts for rupture shape (e.g., Kanamori and Anderson, 1975). Two end-member analytical solutions for C are most often used with equation (4): one for circular ruptures ($r = w = l$), where $C = 7\pi/16$ (Eshelby, 1957), and another for rectangular ruptures ($r = w$), where $C = 2/\pi$ (Knopoff, 1958). The latter constant is used for long ruptures with large aspect ratios (large strike-slip ruptures; Knopoff, 1958), whereas small earthquakes that do not rupture the entire seismogenic thickness are often assumed to be equidimensional ($r \approx w \approx l$; e.g., Yin and Rogers, 1996; Nadeau and Johnson, 1998; Prejean and Ellsworth, 2001; Miller, 2002a,b). To avoid assumptions concerning the shape of the rupture, we use u_{avg}/r as a proxy for stress drop.

General relations between relative CEZ length (s/a and s/b), rupture aspect ratio (a/b), and effective stress drop are displayed in Figure 2. For a given aspect ratio, a decrease in relative CEZ length (s/a or a/b) requires a greater effective stress drop ($\Delta\tau^*$) and thus a relatively stronger CEZ (increase in τ_y/τ_d) to balance the singular near-tip elastic stresses (see discussion in S&F and references therein). Furthermore, for any given relative CEZ length, an increase in aspect ratio requires a slight reduction in $\Delta\tau^*$.

For each individual earthquake we directly measure the CEZ lengths from the distributions of slip and/or stress drop (the latter of which is preferred, see below) determined from the inversions, and use equation (2) along with measured rupture dimensions (a and b) to solve for the ratio of τ_y to τ_d. The absolute magnitudes of τ_d and τ_y are then found by iterating equation (1) until the average slip is matched for the previously determined parameters (CEZ lengths, τ_y/τ_d, and aspect ratios) and estimated material properties. These absolute magnitudes of stress are then used in equation (3) to calculate the effective stress drop.

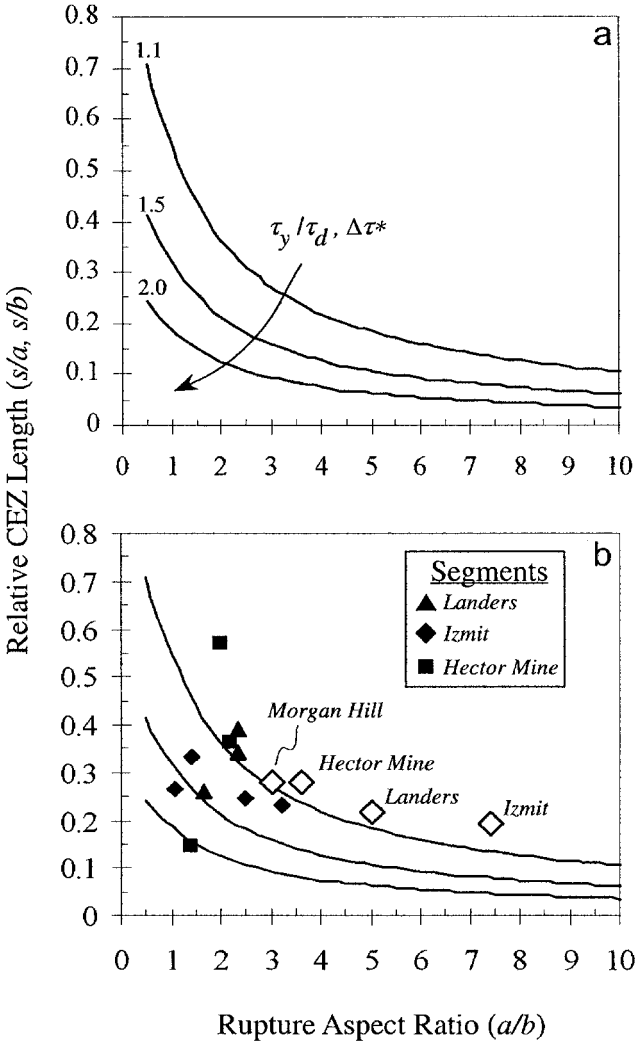

Figure 2. (a) Model predictions (curves) of relative CEZ length (s/a, s/b) versus aspect ratio for ranges of shear yield strength (τ_y)/driving stress (τ_d) that are consistent with earthquake data (shown in b). An increasing ratio of τ_y/τ_d correlates with larger effective stress drops $\Delta\tau^*$. The individual segments (b, filled symbols) all have a smaller range in aspect ratios (1–3) and larger range in relative CEZ lengths (s/a) compared with the composite ruptures (open diamonds). Note the large range in (s/a) for rupture segments with similar aspect ratios.

Source Parameters

The source parameters for continental strike-slip earthquakes used in this analysis are primarily from the compilation of Wells and Coppersmith (1994). We augmented these data (Table 1) with subsurface average slip estimates listed in Mai and Beroza (2000) and parameters for more recent events from slip inversions (e.g., 1999 İzmit and Hector Mine earthquake) (Ji *et al.*, 2002; Delouis *et al.*, 2002) and surface rupture mapping (e.g., Bell *et al.*, 1999; Akyuz *et al.*, 2000; Scientists from the USGS, SCEC and, CDMG 2000; Barka *et al.*, 2002; Lin *et al.*, 2002). By incorporating the former, we are analyzing source parameters that are perhaps more accurate than the ones determined for older events (see Mai and Beroza [2000]). Our database also differs from that of previous researchers (Romanowicz, 1992; Scholz, 1994a,b; Bodin and Brune, 1996; Mai and Beroza, 2000; Shaw and Scholz, 2001) in that we only incorporate events with estimates of rupture width for investigating the scaling of the average slip with the rupture aspect ratio.

Because systematic differences in stress drop (and thus ratios of slip to length) that are expected for intraplate and interplate earthquakes (e.g., Kanamori and Anderson, 1975; Scholz *et al.*, 1986) may create scatter in these data, we attempt to differentiate among these events. We define interplate events as those that occur within a system of faults that comprise the plate boundary (similar to Bodin and Brune [1996], e.g., including 1992 Landers and 1999 Hector Mine earthquakes in southern California) and intraplate events as those that occur in areas geographically distinct from the plate boundary. Using a more rigorous classification scheme that includes information concerning slip rate and recurrence interval (Scholz *et al.*, 1986), the two earthquakes cited previously would be classified as intraplate, but plate boundary related (type 2 of Scholz *et al.*, 1986). Although Scholz (1994b) and Shaw and Scholz (2001) suggested that average slip is systematically three times larger for intra- than interplate earthquakes, we do not find such clear differences (also noted by Bodin and Brune [1996]). In fact, for three examples of intra- and interplate earthquakes with comparable rupture lengths (Table 2), the interplate events have larger magnitudes of slip. Even if we interpret Landers as an intraplate event, the maximum slip to length ratio measured at the surface is considerably larger than other intraplate events with comparable rupture lengths (e.g., 1932 Cedar Mountain, Nevada; Bell *et al.*, 1999). In the following analysis we only use interplate events, as defined previously, but note that the S&F model incorporates variable stress drops ($\approx u_{avg}/l$) among the ruptures. Thus, the distinction between intra- and interplate earthquakes is not critical for this analysis.

Subsurface rupture lengths (l_{ss}) are used when possible because this dimension is commonly greater than the surface rupture length (l_s; Wells and Coppersmith, 1994) and thus is more representative of the rupture dimensions. Average and maximum slip measured at the surface ($u_{avg\text{-}s}$, $u_{max\text{-}s}$) do not always match subsurface averages ($u_{avg\text{-}ss}$) and maxima ($u_{max\text{-}ss}$) that are defined by measurements from instrumentation at near-field and/or teleseismic distances. Therefore, we use the relation determined by Wells and Coppersmith (1994), $u_{avg\text{-}ss} = 0.76 * u_{max\text{-}s}$, for events in which subsurface slip was not determined (Table 1). Subsurface average slip estimates determined from either seismic (strong motion or teleseismic) and/or geodetic inversions (e.g., from Mai and Beroza [2000]) are used when possible and not corrected with the Wells and Coppersmith (1994) relation. Hereafter, we refer to l_{ss} as l and $u_{avg\text{-}ss}$ as u_{avg} unless stated otherwise.

Figure 3 shows coseismic source parameters from our

Table 1
Compilation of Source Parameters Used in This Study (from Wells and Coppersmith [1994], Unless Noted)

Location / Earthquake	Date (mm/dd/yyyy)	Slip Type	Rupture Length (l km)		Rupture Width (km)	Aspect Ratio* (l/w)	Slip (m)		Subsurface† Average Slip (m)	u_{avg}/l (subsurface)
			Surface	Subsurface			Max. (u_{max})	Avg. (u_{avg})		
USA, CA / Fort Tejon	01/09/1857	RL	297		12	24.8	9.4	6.4	7.14	2.41×10^{-5}
USA, CA / Hayward	10/21/1868	RL	48		12	4.0	0.9		0.68	1.43×10^{-5}
USA, CA / San Francisco	04/18/1906	RL	432		12	36.0	6.1	3.3	4.64	1.07×10^{-5}
Turkey / Erzihcan	12/25/1935	RL	360		20	18.0	7.5	1.85	5.70	1.58×10^{-5}
USA, CA / Imperial Valley	05/19/1940	RL	60		11	5.5	5.9	1.5	4.48	7.47×10^{-5}
Turkey / Bolu	02/01/1944	RL	180		20	9.0	3.6	1.8	2.74	1.52×10^{-5}
Turkey / Canakkale	03/18/1953	RL	58		18	3.2	4.35	2.1	3.31	5.70×10^{-5}
Turkey / Abant	05/26/1957	RL	40		8	5.0	1.65	0.55	1.25	3.14×10^{-5}
USA, Alaska / Lituya Bay	07/10/1958	RL	200	350	12	29.2	6.6		5.02	1.43×10^{-5}
USA, CA / Parkfield	06/28/1966	RL	38.5	35	10	3.9	0.2		0.15	3.95×10^{-6}
Turkey / Varto	08/19/1966	RL	30		10	3.0	0.4	0.15	0.30	1.01×10^{-5}
Turkey / Mudurna Valley	07/22/1967	RL	80		20	4.0	2.6	1.63	1.98	2.47×10^{-5}
USA, CA / Borrego Mountain	04/09/1968	RL	31	40	10	4.0	0.38	0.18	0.29	7.22×10^{-6}
Iran / Dasht-e-Bayaz	08/31/1968	LL	80	110	20	5.5	2.3	4.00	1.75	1.59×10^{-5}
USA, Alaska / Sitka‡	07/30/1972	RL		180	10	18.0		6.00	6.00	3.33×10^{-5}
USA, CA / Galway Lake	05/31/1975	RL	6.8	5	15	0.5	0.02		0.02	2.24×10^{-6}
Guatemala / Motagua	02/04/1976	LL	235	257	13	19.8	3.4	2.6	2.58	1.01×10^{-5}
Turkey / Caldiran	11/24/1976	RL	55		18	3.1	3.5	2.05	2.66	4.84×10^{-5}
Iran / Bob Tangol	12/19/1977	RL	12	14	12	1.2	0.3	0.12	0.23	1.63×10^{-5}
USA, CA / Homestead Valley	03/15/1979	RL	3.9	6	4	1.5	0.1	0.05	0.08	1.27×10^{-5}
USA, CA / Coyote Lake§	08/06/1979	RL	14.4	14	10	1.4	0.15		0.114	7.92×10^{-6}
USA, CA / El Centro§	10/15/1979	RL	30.5	51	12	4.3	0.8	0.18	0.62	1.19×10^{-5}
USA, CA / Morgan Hill‖	04/24/1984	RL		28.5	12	2.4	2.31	0.26	0.26	9.12×10^{-6}
USA, CA / Elmore Ranch§	11/24/1987	LL	10	30	12	2.5	0.2		0.28	9.33×10^{-6}
USA, CA / Superstition Hill§	11/24/1987	RL	27	30	11	2.7	0.92	0.54	1.00	3.33×10^{-5}
USA, CA / Landers#	06/28/1992	RL	70	78	15	5.2	7.94	2.39	2.39	3.06×10^{-5}
USA, CA / Landers**	06/29/1992	RL	70	80	16	5.0	5.34	1.62	1.62	3.06×10^{-5}
Turkey / İzmit††	08/17/1999	RL	120	155	21	7.4	5.65	1.80	1.80	1.16×10^{-5}
Turkey / Duzce‡‡	11/12/1999	RL		55	20	2.8	1.5	1.00	1.14	2.07×10^{-5}
USA, CA / Hector Mine§§	10/16/1999	RL	40	54	15	3.6	8.2	2.35	2.35	4.35×10^{-5}
China / Kunlun‖‖	11/14/2001	LL	400				16.3	6.60		

*Values are calculated from subsurface data when possible and surface data in other instances.

†Values are calculated from surface ruptures using $u_{avg\text{-}ss} = 0.76 * u_{max\text{-}s}$ (determined by Wells and Coppersmith, 1994), unless estimates were determined by geophysical techniques.

‡Average subsurface displacement from Schell and Ruff (1989).

††Parameters from Delouis *et al.* (2002), except surface rupture length from Barka *et al.* (1999).

§Average subsurface displacement from Mai and Beroza (2000).

‖Parameters from Beroza and Spudich (1988) and Beroza and Mikumo (1996).

#Parameters from Wald and Heaton (1994), except surface rupture length from Sieh *et al.* (1993).

**Parameters from Peyrat *et al.* (2001), except surface rupture length from Sieh *et al.* (1993).

‡‡Parameters from Tibi *et al.* (2001), except surface rupture length from Akyuz *et al.* (2000)

§§Parameters from Ji *et al.* (2002), except surface rupture length from scientists from the USGS, SCEC, and CDMG (2000).

‖‖Parameters from Lin *et al.* (2002).

revised compilation of continental, interplate strike-slip earthquakes (Table 1). Two forms of the data are displayed, u_{avg} versus length (Fig. 3a) and u_{avg} versus aspect ratio (Fig. 3b), using subsurface lengths wherever possible. Logarithmic curves fit to the data exhibit similar, but slightly higher correlation coefficients than linear fits in each plot (Fig. 3c and d), suggesting that the relation is only slightly better interpreted as nonlinear. The logarithmic relation between u_{avg} and rupture aspect ratio has the highest correlation coefficient, and slip appears to roll over (or increase at reduced rates) for aspect ratios $>\sim 6$. Although earthquakes with rupture lengths <120 km or aspect ratios <6 appear to exhibit a systematic relationship to u_{avg}, the correlation is actually worse for these earthquake dimensions than for the entire range (Fig. 3e and f). Furthermore, u_{avg} is even less correlated to rupture width (plot not shown) for these ruptures.

Source parameters displayed in Table 1 and Figure 3 are from large earthquakes, in other words, $l \gg w$. If the W model were correct, u_{avg} would remain constant for all rupture lengths. If the L model were correct, u_{avg} would increase for all rupture lengths. The earthquake data presented in Figure 3 appear partially consistent with the L model because, in general, slip is larger on longer ruptures. However, the

Table 2
Source Parameter Comparison for Intraplate and Interplate Earthquakes with Similar Lengths

Location / Earthquake	Date (mm/dd/yyyy)	Slip Type	Tectonic Setting	$\mathbf{M}_w$ (moment magnitude)	Rupture Length (l, km)		Rupture Width (km)	Slip (m)*	
					Surface	Subsurface		Max. (u_{max})	Avg. (u_{avg})
Turkey / Duzce[†]	10/12/1999	RL	Interplate	7.2	55	55	20	4^{s} [†]	1.6^{ss}
China / Daofu[‡]	01/23/1981	LL	Intraplate	6.64	44	46	15	1.5	
USA, CA / Landers[§]	06/28/1992	RL	Interplate	7.34	70	78	15	7.94^{ss} (6^{s})	2.39^{ss}
USA, Nevada / Cedar Mountain[‡‖]	12/21/1932	RL	Intraplate	6.83	75	75	15	2	
Iran / Dasht-e-Bayaz[‡]	08/31/1968	LL	Interplate	7.23	80	110	20	5.2	2.30
China / Luhuo[‡]	02/06/1973	LL	Intraplate	7.47	89	110	13	3.6	1.3

*Measurements from surface rupture mapping (s) and subsurface determinations (ss) are indicated; unmarked are unknown. Max., maximum; Avg., average.

[†]Parameters from Tibi *et al.* (2001), except surface rupture length from Akyuz *et al.* (2000).

[‡]Parameters from Wells and Coppersmith (1994).

[§]Parameters from Wald and Heaton (1994), except surface rupture length from Sieh *et al.* (1993).

[‖]Parameters from Bell *et al.* (1999).

data also appear partially consistent with a W model because, for long ruptures, the ratio of slip to length is less than some shorter ruptures. Considerable scatter exists in these plots, but what should be clear is that no single curve provides a good fit to the relationship between u_{avg} and l or u_{avg} and the aspect ratio (l/w) shown in Figure 3. In other words, based on these data, one can only predict a range of average slip for a given rupture length or aspect ratio.

Comparison between 3D CEZ Model and Earthquake Source Parameters

In this section we compare the S&F model with the observed source parameters (Table 1 and Fig. 3). Using equation (1), we plot u_{avg} against the aspect ratio for a range of rupture lengths, while keeping $w = 15$ km (~average from data), and compare this with our new compilation of earthquake parameters (Fig. 4). Each curve in Figure 4 represents a constant τ_y/τ_d ratio, which requires a slight decrease in effective stress drop for larger aspect ratios (see equation 3). In these models, with $w = 15$ km, the strongest rollover occurs between aspect ratios of ~1–5 (Fig. 4a), and the curves exhibit similar shapes as those calculated with use of different methods by Bodin and Brune (1996), Yin and Rodgers (1996), and Shaw and Scholz (2001). These aspect ratios are larger than predicted by the W model, where a scaling change would occur at an aspect ratio of 1 if rupture were equidimensional. If $w < 15$ km, the rollover region would occur at smaller aspect ratios, whereas if $w > 15$ km, the rollover region would occur at larger aspect ratios.

Significant variability in u_{avg} is apparent for events with comparable dimensions, and, if real, suggests that the total rupture dimension is not the only factor that influences the magnitude of average slip. As pointed out by Bodin and Brune (1996) and Mai and Beroza (2000), these differences require variations in stress drop. Observations indicate that slip and stress drop are spatially heterogeneous along the rupture surface (e.g., Papageorgiou and Aki, 1983a,b; Heaton, 1990; Zeng *et al.*, 1993; Wald and Heaton, 1994; Mikumo and Miyatake, 1995; Beroza and Mikumo, 1996; Olsen *et al.*, 1997; Peyrat *et al.*, 2001), and Mai and Beroza (2000), Shaw and Scholz (2001), and Miller (2002b) suggested that these heterogeneities add variability to general scaling properties. To overcome this dilemma when attempting to fit the data with a single function, Mai and Beroza (2000) analyzed the scaling of source parameters based on the effective rupture dimensions. These represent statistically determined rupture sizes that account for areas of low slip, and thus an effective rupture area that is less than the total rupture area. After making this correction they found that the data generally support a W model for the longest strike-slip earthquakes, although slip continued to increase—at reduced rates—for the largest ruptures. Both dynamic numerical models that incorporate some form of slip and/or velocity weakening (Shaw and Scholz, 2001; Miller, 2002a,b), static numerical (Bodin and Brune, 1996), and analytical (Yin and Rodgers, 1996) models with total stress drop show similar results despite the fact that these zones of small slip are not treated as in Mai and Beroza (2000).

These areas of low slip have important physical consequences for strong ground motions (Aki, 1979; Papageorgiou and Aki, 1983a,b; Zeng *et al.*, 1993) and, we believe, may lend insight to the scaling paradox of strike-slip faults. Instead of scaling down the length to account for these low-slip regions (as in the analysis of Mai and Beroza [2000]), we incorporate them when evaluating the average source parameters and investigate whether differences in source parameter scaling can be explained by variations in the size of low-slip, negative stress drop regions, that we interpret as CEZs.

As the variability in u_{avg}/l is proportional to average stress drop (equations 3–4), a plot of u_{avg}/l against aspect ratio would clearly illustrate the variability in stress drop for a given rupture aspect ratio. In fact, the variability in u_{avg}/l (equation 3) for all aspect ratios is significant (Fig. 5). For a given τ_y/τ_d ratio, the largest *range* of stress drops occurs

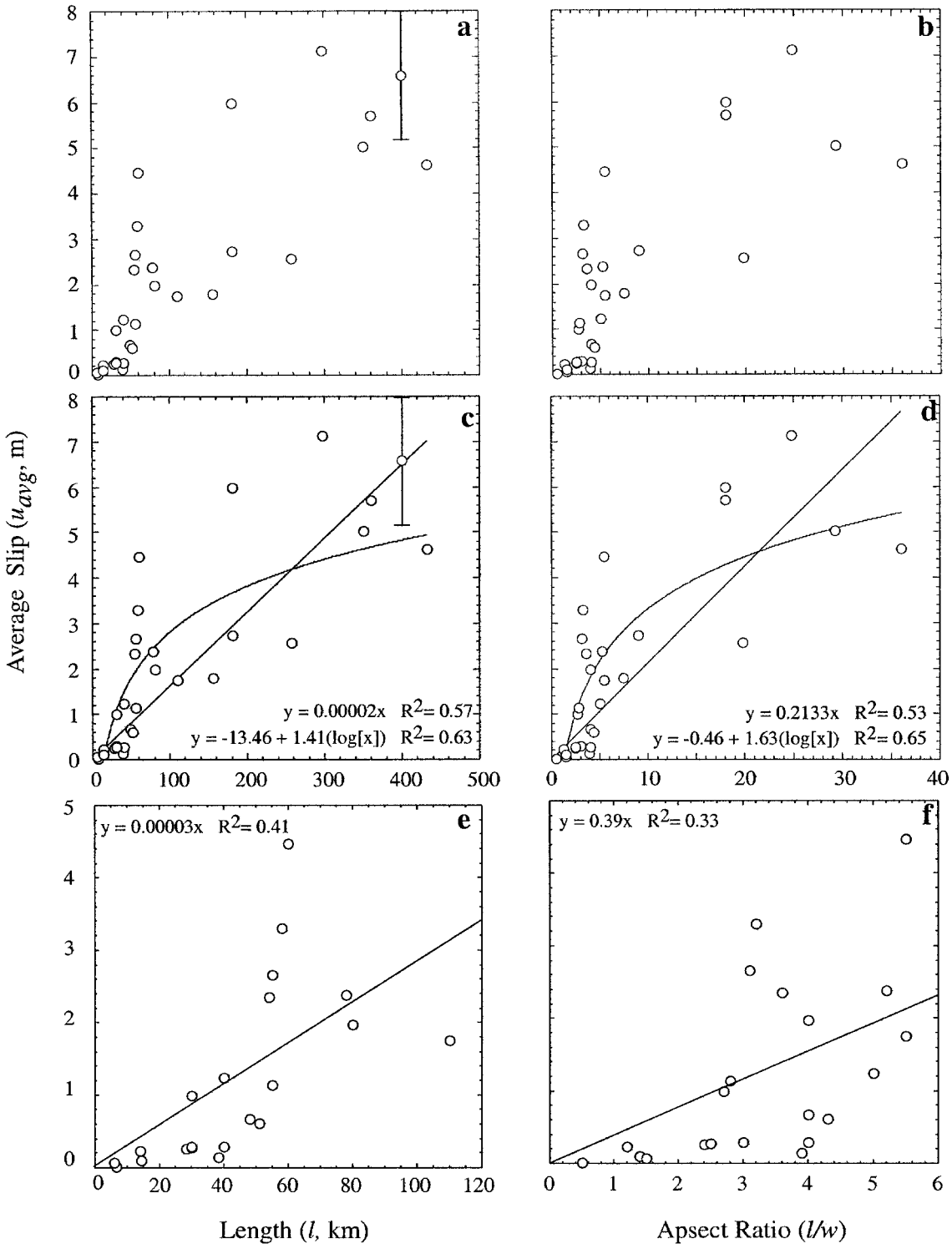

Figure 3. Coseismic source parameters from our revised compilation of continental, interplate strike-slip earthquakes (Table 1). Average displacement (u_{avg}) is plotted against length (a) and aspect ratio (b), with subsurface length l_{ss} plotted when possible. Logarithmic fits have higher correlation coefficients (R^2 = 0.63 [c] and 0.65 [d]) than linear fits (R^2 = 0.57 [c] and 0.53 [d]). Close up of (c) and (d) for ruptures with l_{ss} <120 km (e) and aspect ratios <6 (f) show no correlation with u_{avg} for a linear fit to the data. Data point with error bars in (a) and (c) is from 2001 Kunlun, Tibet, earthquake (Lin *et al.*, 2002) and is not used in statistical fit because the depth is not well known.

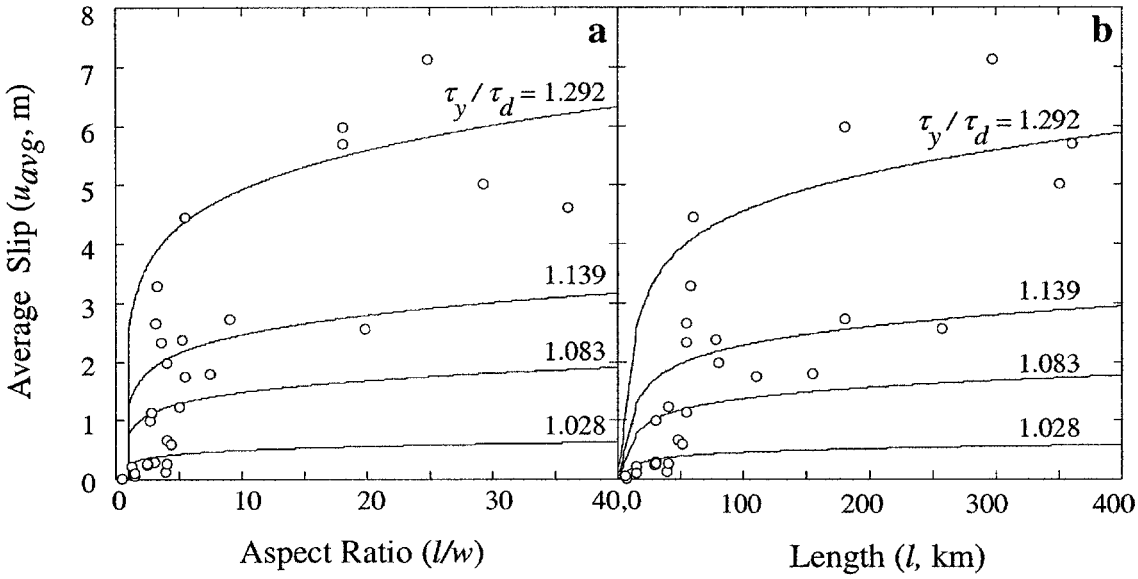

Figure 4. Model predictions (curves) of average slip versus aspect ratio (a) and length (b) for the same range of shear yield strength (τ_y)/driving stress (τ_d) displayed in Figure 5. At aspect ratios of one, τ_y/τ_d of 1.292 = $\Delta\tau^*$ of 10 MPa, 1.139 = $\Delta\tau^*$ of 5 MPa, 1.083 = $\Delta\tau^*$ of 3 MPa, and 1.028 = $\Delta\tau^*$ of 1 MPa. Note that when the model predictions are displayed in this form, no single scaling law is capable of explaining the full range of data.

for ruptures with aspect ratios $<\sim 5$, whereas stress drops for large-aspect-ratio earthquakes are smaller and do not exhibit a wide range in magnitude (Fig. 5a). This relationship is consistent with the earthquake data plotted in Figure 5b. For the case of depth-limited ruptures, a constant τ_y/τ_d in equation (3) results in an effective stress drop ($\Delta\tau^*$, or $\sim u_{avg}/l$) that asymptotically decreases with increasing aspect ratio (Fig. 5).

Large variations in stress drop have been observed by numerous researchers (Kanamori and Anderson, 1975; Hanks, 1977; Abercrombie, 1995; Nadeau and Johnson, 1998; Prejean and Ellsworth, 2001). For example, Prejean and Ellsworth (2001) observed stress drops of ~0.01–30 MPa over a range in seismic moment from $\sim 10^9$ to 10^{15} N m (10^{16}–10^{23} dyne cm) from 2 km depth in a borehole at Long Valley Caldera, California. Furthermore, Nadeau and Johnson (1998) observed stress drop to decrease systematically with increasing seismic moment, from $\sim 10^5$ to 10^2 bars of stress drop ($\Delta\sigma$) and $\sim 10^{15}$ to 10^{25} dyne cm (10^8–10^{18} N m) of seismic moment (M_0), according to the following empirical relationship, $\log(\Delta\sigma) = 8.19 - 0.25 \log(M_0)$. This observed dependence of stress drop on seismic moment is from sequences of repeating earthquakes along the Parkfield segment of the San Andreas fault, California, and spans a range in magnitude (M_w) from -0.7 to 6. Although Beeler *et al.* (2001) offer an alternative hypothesis to the interpretation of Nadeau and Johnson (1998) the data still require a variation in stress drop. Heaton's (1990) self-healing slip-pulse model, which incorporates velocity-dependent slip-weakening behavior, predicts results similar to Nadeau and Johnson (1998): rupture pulses arrested over short distances produce relatively high static stress drops, whereas pulses that travel longer distances produce lower stress drops. The earthquake data analyzed in this study exhibit a large range of stress drops for ruptures with aspect ratios $<\sim 6$ (Figs. 3 and 4), which is especially apparent when plotted in u_{avg}/l–aspect ratio space (Fig. 5b). We hypothesize that the range of stress drop and aspect ratios are directly related to variations in end-zone size, and thus to absolute magnitudes of shear driving stress and yield strength in the CEZ model. We explicitly test this model by measuring the end-zone size from 2D distributions of stress drop and slip from four well-studied earthquakes.

CEZ Observations from Inversions for Slip and Stress Drop

We compare average source parameters with CEZ lengths determined from slip and stress drop distributions of the following strike-slip earthquakes: 1999 İzmit (M_w 7.4), Turkey (Delouis *et al.*, 2002); 1999 Hector Mine (M_w 7.1), California (Ji *et al.*, 2002); 1992 Landers (M_w 7.2), California (Wald and Heaton, 1994; Peyrat *et al.*, 2001); and 1984 Morgan Hill (M_w 6.3), California (Beroza and Spudich, 1988; Beroza and Mikumo, 1996). Slip and stress drop distributions for three of these ruptures are based on joint kinematic and dynamic inversions of some combination of geologic, geodetic, and seismic recordings of the deformation, including GPS and InSAR data, field mapping of surface slip vectors, strong motion and teleseismic records. The in-

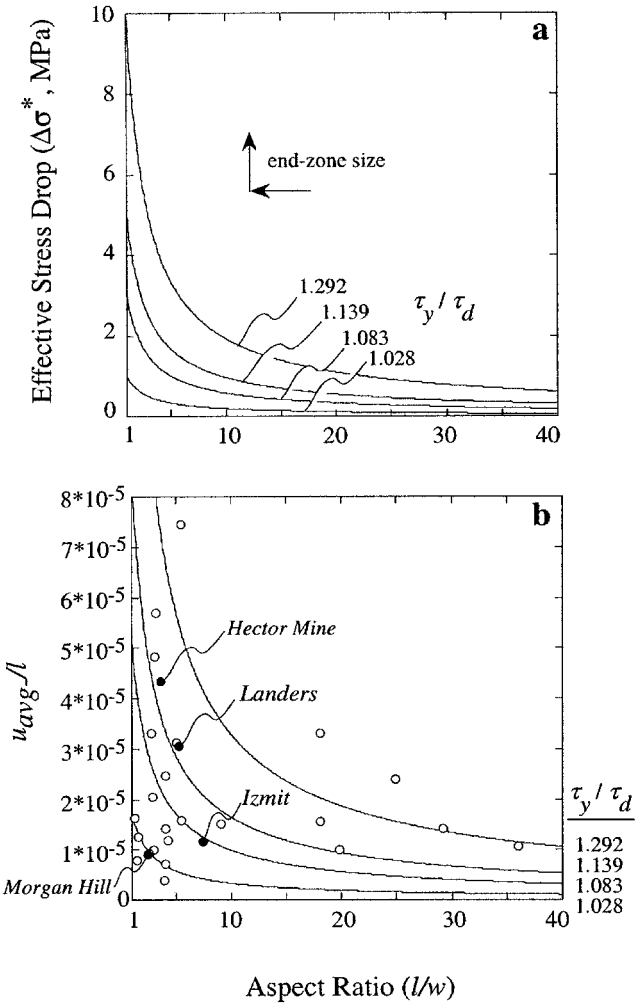

Figure 5. Effective stress drop (a) and u_{avg}/l (b) versus aspect ratio for a range of shear yield strength (τ_y)/driving stress (τ_d) ratios that are compatible with the compiled earthquake data. Earthquakes analyzed in this study (Tables 1 and 3) are indicated in (b). Note that the model predicts smaller relative end zone lengths for İzmit than the Landers or Hector Mine earthquakes and larger end zone lengths for Morgan Hill relative to İzmit.

version for the 1984 Morgan Hill earthquake is based on strong-motion data alone. The spatial resolution of these inversions is ~3.0 * 2.5 km (along-strike * down-dip subfault lengths) for Hector Mine and Landers (kinematic solution from Wald and Heaton [1994], and the dynamic solution of Peyrat *et al.* [2000] contains a grid spacing of 200 m), to 0.5 * 1.0 km for Morgan Hill and 7.5 * 4.5 km for İzmit.

We recognize that the measured CEZ lengths are highly dependent on the quality of the inversions. To mitigate these effects, we analyze slip events that were recorded with a dense array of instruments and, that preferably are based on joint inversions of multiple data types. Sensitivity analyses indicate that the latter significantly enhances the resolution (Wald and Graves, 2001; Delouis *et al.*, 2002). Furthermore, we reduce the errors by interpreting CEZ dimensions from depth-averaged data and only determine the CEZ lengths in the along-strike direction because the relative resolution of the CEZ is significantly reduced in the down-dip direction (*b*). These models have greater uncertainty in depth than along-strike, especially at the deeper levels (Ji *et al.*, 2002; Delouis *et al.*, 2002), and a high probability also exists for relatively larger variations in stress or frictional strength with depth than along-strike.

Three of these earthquakes comprise multiple rupture segments (İzmit [four segments], Hector Mine [three segments], and Landers [three segments]), and each of the inversions consists of multiple-segment models except for Landers. This raises another significant issue; all the average source-scaling analyses treat ruptures as occurring along a single fault segment, whereas many of the larger ruptures consist of multiple-rupture segments. Thus we analyze the CEZ lengths and source parameters from both the composite rupture and individual segments. For both the composite ruptures and individual segments, the total CEZ length consists of numerous patches that are added together to estimate 2*s*.

A direct measurement of CEZ lengths is attainable from the distributions of negative stress drop (Fig. 1). Stress drop distributions for the Landers and Morgan Hill earthquakes are based on dynamic models, which are not presently available for the others. Spatial distributions of dynamic stress drop are calculated from a combination of the slip distribution (derived in kinematic models), rupture time and rise time, obtained from waveform inversion, under the assumption of a friction law and initial stress field. Although dynamic models include more parameters and assumptions, the spatial patterns of slip produced from kinematic models, in general, correlate with stress drop (and slip) distributions determined from dynamic models (Figs. 6 and 7). This correlation provides a basis on which to estimate CEZ sizes from slip distributions alone, although we note that the stress drop distributions are preferred because they provide an objective method for measuring CEZ sizes (see following text).

Average slip and stress drops were calculated in the along-strike directions (i.e., *a*) from each inversion and used to measure CEZ lengths, which are highlighted in gray for each average slip distribution (Figs. 6–9, tabulated in Table 3). For the Landers and Morgan Hill earthquakes, CEZs were measured from the regions where average stress drops are negative. For these two ruptures, the areas of relatively low slip and negative stress drop are similar. However, regions of negative stress drop at rupture segment boundaries have relatively larger slip than at the initial and final fault tips of the Landers rupture (Fig. 6). This relationship is also apparent for the Morgan Hill inversion (e.g., see $x = 9$ and 17 km from northwest) although they do not occur at recognized segment boundaries. This indicates that CEZs are represented not only by regions of low slip, but by regions of relatively low slip that are represented by troughs in the average slip distribution. For this reason, we feel that measuring CEZ

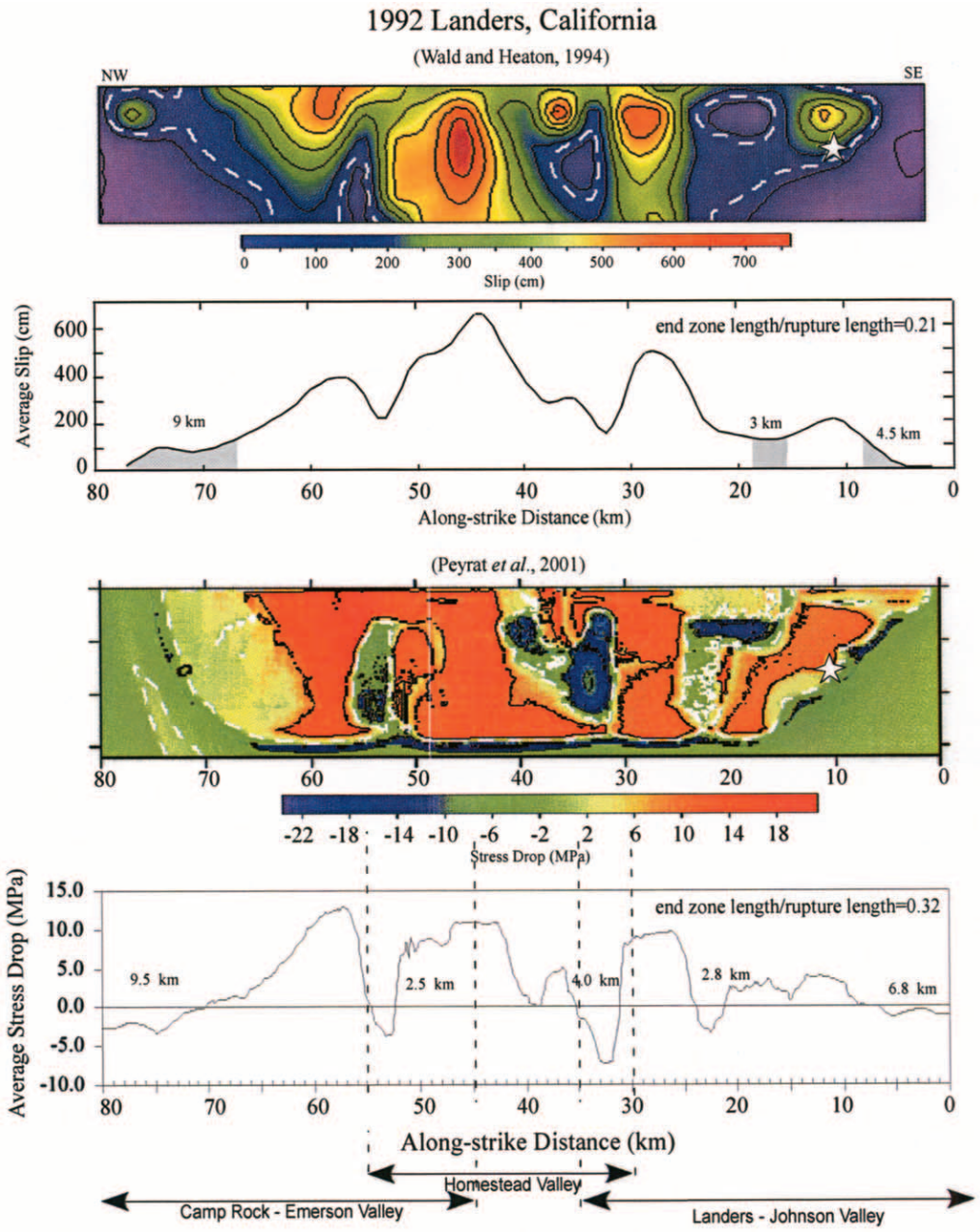

Figure 6. Three-dimensional distributions of slip (top, 100-cm contours) and stress drop (bottom) estimated for the 1992 Landers (M_w 7.2), California, earthquake from kinematic (Wald and Heaton, 1994) and dynamic (Peyrat *et al.*, 2001) inversions, respectively. Depth-averaged, along-strike distributions are provided below each 2D plot. CEZs are defined by gray areas in average slip plots and all areas with negative numbers in average stress drop plates. The white dashed lines (in 3D slip distributions) represent the values of u_{CEZ} at the tail of the CEZ (see Table 3) or the zero stress drop contour. All distributions have been projected onto a single vertical plane. The white star represents the hypocenter location.

lengths from slip distributions alone are subject to greater errors.

For the Morgan Hill earthquake, the along-strike CEZ length defined from stress drop is less than that estimated from the kinematic slip distribution (~7.8 km versus ~11.2 km; Fig. 7). The difference arises because slip may still accumulate in regions of negative stress drop, and the slip magnitude depends on the rupture energy (i.e., available strain energy), which is a function of initial stress conditions and frictional behavior (Olsen *et al.*, 1997; Peyrat *et al.*, 2001). In other words, as the rupture front enters an unstressed region the rupture arrest is smoother in dynamic models than

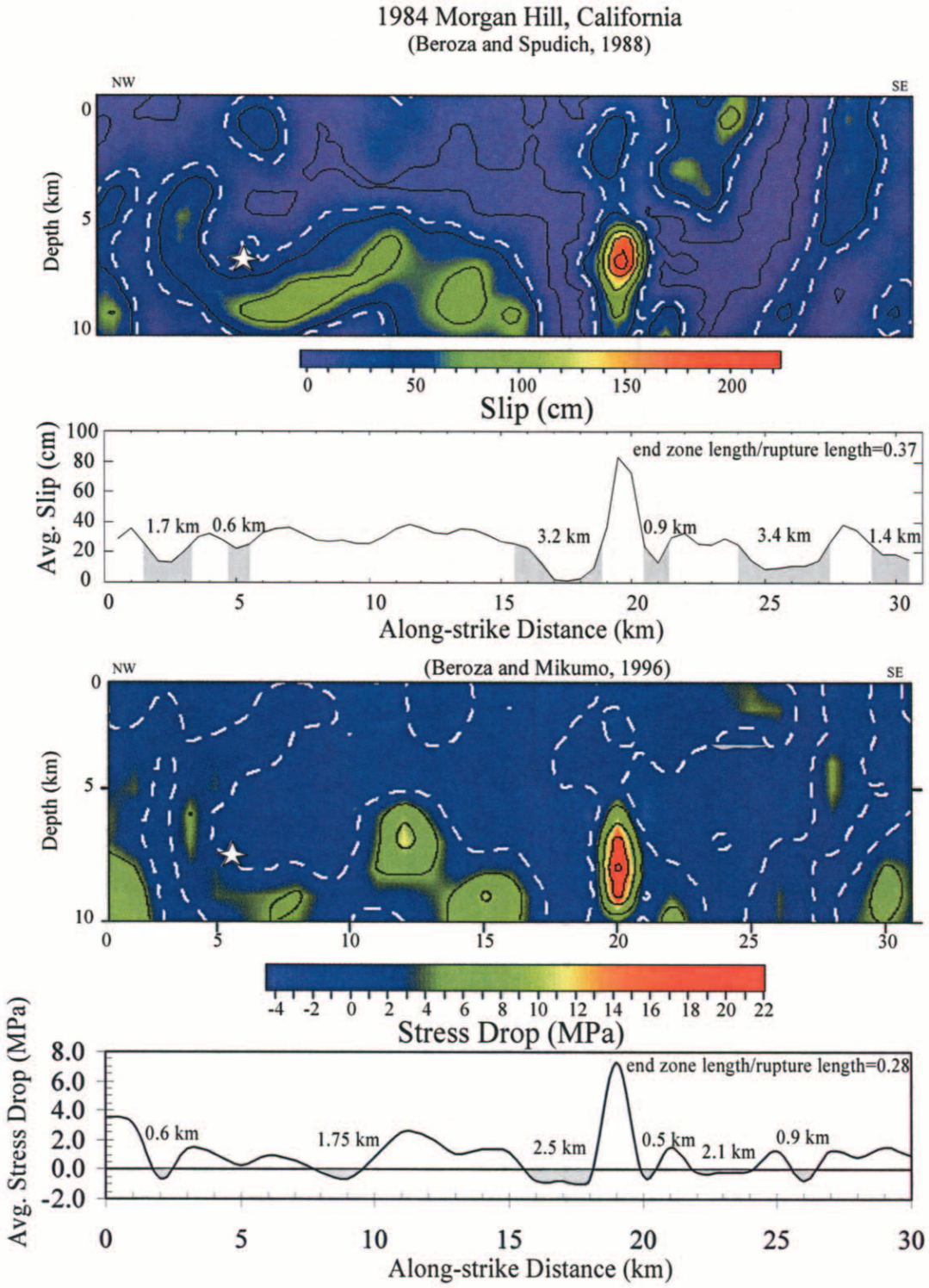

Figure 7. Three-dimensional distributions of slip (top, 40-cm contours) and stress drop (bottom) estimated for the 1984 Morgan Hill (M_w 6.3), California, earthquake from kinematic (Beroza and Spudich, 1988) and dynamic (Beroza and Mikumo, 1996) inversions, respectively. Details are the same as described for Figure 6.

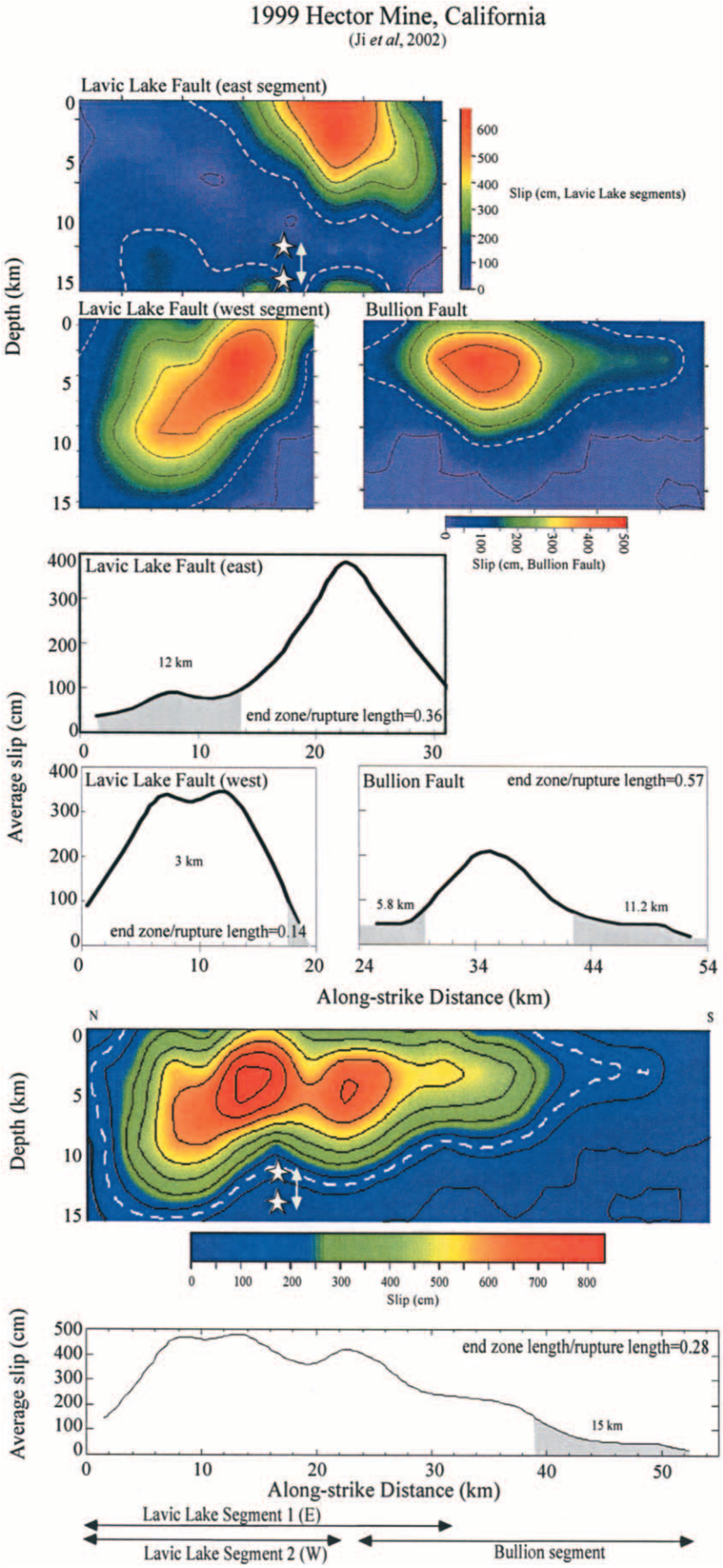

Figure 8. Three-dimensional distributions of slip for individual segments (top, 100-cm contours) and composite rupture (bottom, 100 cm) estimated for the 1999 Hector Mine (M_w 7.1), California, earthquake from joint kinematic inversions (Ji *et al.*, 2002). Details are the same as described for Figure 6. A range of preferred hypocenter depths (white stars, 12.1–14.8 km) from Ji *et al.* (2002) is displayed.

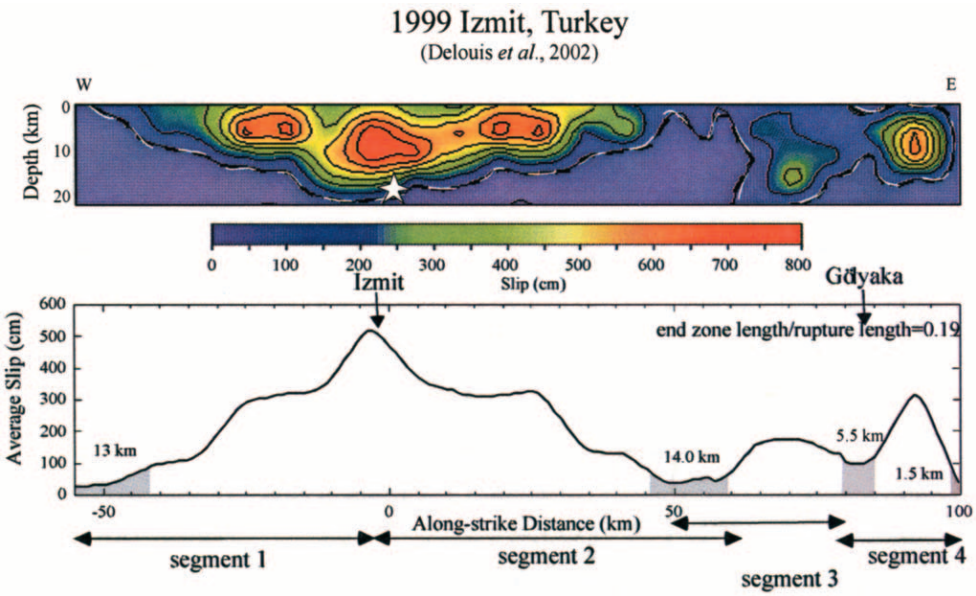

Figure 9. Three-dimensional distributions of slip (100-cm contours) estimated for the 1999 İzmit (M_w 7.4), Turkey, earthquake from joint kinematic inversion of Delouis *et al.* (2002). Slip distributions have been projected onto a single vertical plane.

Table 3
CEZ Dimensions, Coseismic Source Parameters, and Stress

Earthquake	$u_{avg\text{-}ss}$ (m)	Length ($2a$, km)	Width ($2b$, km)	Aspect Ratio (l_{ss}/w)	$u_{avg\text{-}ss}/L$ ($2a$) ($\times 10^5$)	σ_y/σ_d (MPa)	σ_y (MPa)	σ_d (MPa)	Effective Stress Drop ($\Delta\tau^{\pm}$, MPa)	Knopoff Stress Drop (MPa)	s/a	$2s$ (a, km)	u_{CEZ} (m)	Error a (±) km	Error s/a (±)	Error b (±) km	Error s/b (±)
1999 İzmit*	1.80	155.0	21	7.4	1.161					1.8	0.22	34.0		3.75	0.0242	2.25	0.11
Segment 1	2.18	52.5	21	2.5	4.152	1.8	16.7	9.1	1.2	2.2	0.25	13.0	1.40	3.75	0.0714		
Segment 2	2.22	67.5	21	3.2	3.289	1.8	16.1	8.8	1.0	2.2	0.21	14.0	1.32	3.75	0.0556		
Segment 3 (Karadere)	1.11	30.0	21	1.4	3.700	2.1	10.0	4.8	1.1	1.1	0.28	8.5	0.77	3.75	0.1250		
Segment 4 (Duzce)	1.71	22.5	21	1.1	7.600	2.2	19.0	8.8	2.2	1.7	0.31	7.0	1.22	3.75	0.1667		
1999 Hector Mine†	2.35	54.0	15	3.6	4.352					3.3	0.28	15.0		1.50	0.0278	1.25	0.08
Lavic Lake (East Fault 1)	1.59	33.0	15	2.2	4.818	1.6	19.9	12.7	1.4	2.2	0.36	12.0	1.21	1.50	0.0455		
Lavic Lake (West Fault 2)	2.26	21.0	15	1.4	10.762	3.0	29.9	10.0	3.2	3.2	0.14	3.0	1.12	1.50	0.0714		
Bullion (East Fault 3)	0.91	30.0	15	2.0	3.033	1.3	18.3	14.4	0.9	1.3	0.57	17.0	0.89	1.50	0.0500		
1992 Landers‡	2.39	78.0	15	5.2	3.064					3.3	0.22	16.5		1.50	0.0192	1.25	0.08
1992 Landers§	1.62	80.0	16	5.0	2.025					2.1	0.32	25.6		1.50	0.0188	1.25	0.08
Cumprock-Emerson Segment	2.28	35.0	15	2.3	6.514	1.6	29.0	18.0	1.9	3.2	0.34	12.0	1.71	1.50	0.0429		
Homestead Valley Segment	2.77	25.0	15	1.7	11.080	2.0	30.0	15.0	3.2	3.9	0.26	6.5	1.76	1.50	0.0600		
Landers-Johnson Valley Segment	1.78	35.0	15	2.3	5.086	1.5	24.0	16.0	1.5	2.5	0.39	13.6	1.39	1.50	0.0429		
1984 Morgan Hill‖	0.26	30.0	10	3.0	0.867					0.5	0.37	11.2		0.25	0.0083	0.5	0.05
1985 Morgan Hill#	0.26	30.0	10	3.0	0.867	1.1	31.0	28.2	0.5	0.5	0.28	8.4		0.25	0.0083	0.5	0.05

*Data from kinematic model of Deluois *et al.* (2002).
†Data from kinematic model of Ji *et al.* (2002).
‡Data from kinematic model of Wald and Heaton (1994).
§Data from dynamic model of Peyrat *et al.* (2001).
‖Data from kinematic model of Beroza and Spudich (1988).
#Data from dynamic model of Beroza and Mikumo (1996).

for kinematic models (Peyrat *et al.*, 2001). In contrast to observations from Morgan Hill, the along-strike CEZ length defined from stress drop for Landers is greater than that estimated from the kinematic slip distribution (~25.6 km versus ~16.5 km; Fig. 9). The primary difference between the CEZ lengths determined from slip and stress drop is that regions of relatively small slip at segment boundaries were not considered as CEZs despite an association with negative stress drops, indicating that they represent CEZs.

The curvature of the average slip distribution is used to define the CEZ lengths by defining the CEZ tail as the location where the curvature changes from concave up to concave down in regions of small slip magnitude (Fig. 1). In general, the slip magnitude at the CEZ tail appears remarkably consistent across the entire rupture (Landers and Morgan Hill) or each segment (İzmit and Hector Mine). However, for the İzmit segment, where we only have access to the data projected onto a single plane (despite the rupture and model comprising multiple segments), there is a special case where slip at the CEZ tail is notably larger. Between segments 3 and 4 the slip is higher than that within the other end zones, and we infer that it likely represents a combination of small slip on two overlapping segments. Although overlapping surface ruptures were not observed, inversions indicate that the bulk of slip on these segments is deeper and thus the fault geometry, determined primarily from surface-rupture patterns, is not well defined. Similar examples of large slip at segment boundaries are also apparent in the single-fault models for the Landers and Hector Mine ruptures.

Despite the aberrations at segment boundaries, notice that in each case the CEZ defined by the observations and our interpretation agrees well with the previous definition provided here and in earlier studies: regions where slip and slip gradients dramatically decrease from larger values in the central or yielded portion of the fault (region $2c$, Fig. 1), where slip tapers to zero toward the fault tip (region s). We emphasize that this standard interpretation of the CEZ (e.g., Rudnicki, 1980; Scholz and Cowie, 1992) is closer to the concept of a barrier (with small slip) provided by Aki (1979) and Papageorgiou and Aki (1983a,b) than what they refer to as an "end zone" defined by f_{max} (see following discussion).

A summary of the measured CEZ lengths for each individual rupture segment and composite ruptures are provided in Table 3. The u_{avg}/l ratios for both the composite ruptures and individual segments of the Landers, Hector Mine, and İzmit events exhibit a general negative dependence with the measured CEZ lengths (Fig. 10), with two apparent outliers. The first outlier is segment 3 of İzmit, for which the CEZ is likely to be underestimated because we did not include a CEZ at the eastern end of this segment. As discussed previously, if this segment extends further east in the subsurface the CEZ is likely to increase. Increasing the CEZ length from 8.5 km to 14.0 km by including the region of low slip just beyond its eastern tip (Fig. 9) would rectify this outlier to be in accord with the remainder of the data. The other obvious outlier is the Morgan Hill event, whether CEZ length is determined from stress drop or slip. The inversion for this rupture is the only one that is not based on joint methods (strong-motion data alone). Another apparent difference from others in this study is the interseismic behavior of its host fault. This portion of the Calaveras fault is currently creeping at a rate of 14 ± 2 mm yr^{-1}, (Galehouse and Lienkaemper, 2003) similar to its geologic (Holocene) rate of 14 ± 5 mm yr^{-1} (Kelson *et al.*, 1999), despite hosting significant earthquakes. If a significant amount of the accumulated elastic strain energy is released aseismically, the stress drop during seismic rupture would presumably be reduced relative to ruptures of equivalent size along locked faults that have similar slip rates and do not creep.

The negative dependence of u_{avg}/l on CEZ length ($2s$) for individual rupture segments is required by the S&F model and indicates that, for faults with similar rupture dimensions, a difference in stress drop is related to the size of the CEZ. Linear regressions of u_{avg}/l ($\times 10^5$) on $2s$ (kilometers) for individual rupture segments (excluding Morgan Hill) indicate $u_{avg}/l = -0.579 \times (2s) + 12.16$ ($R^2 = 0.70$), or $u_{avg}/l = -0.643 \times 2s + 13.21$ ($R^2 = 0.88$) if the CEZ length of segment 3 from İzmit is increased from 8.5 km to 14 km. Although the relation between u_{avg}/l and CEZ length for composite ruptures provides the best fit (including the stress drop model for Landers, but excluding Morgan Hill), with $u_{avg}/l = 0.213(2s) + 7.53$ ($R^2 = 0.99$), we later discuss reasons why this model is not preferred. The constants for the fit between u_{avg}/l and $2s$ may be redefined upon the collection of more data and/or higher resolution attained in future inversions.

Absolute Magnitudes of Shear Stress

For the measured rupture dimensions ($2a = l$ and $2b = w$) and half-CEZ length (s), we solve for the τ_d/τ_y ratio with equation (2). We then iterate the absolute magnitude of stresses with equation (1) by using the aforementioned parameters and elastic material properties, until convergence is achieved with the measured u_{avg} (determined from published slip inversions). Once convergence is achieved, slip at the tail of the CEZ (u_{cez}) and stress drops were recorded for each event (Table 3). Using this method, we find that estimated magnitudes of shear driving stress and yield strength are remarkably similar among the individual rupture segments within each earthquake sequence, and for all the data combined. Results are graphically displayed in Figure 11 for the Landers earthquake and the other events are located in the appendix; all results are tabulated in Table 3. Similar magnitudes are estimated despite significant differences in average slip and CEZ lengths among the segments (Fig. 11 and Table 3). Although these calculations are based on average CEZ lengths that are likely to be quite robust, error estimates are shown in Figure 11 and Table 3 for along-

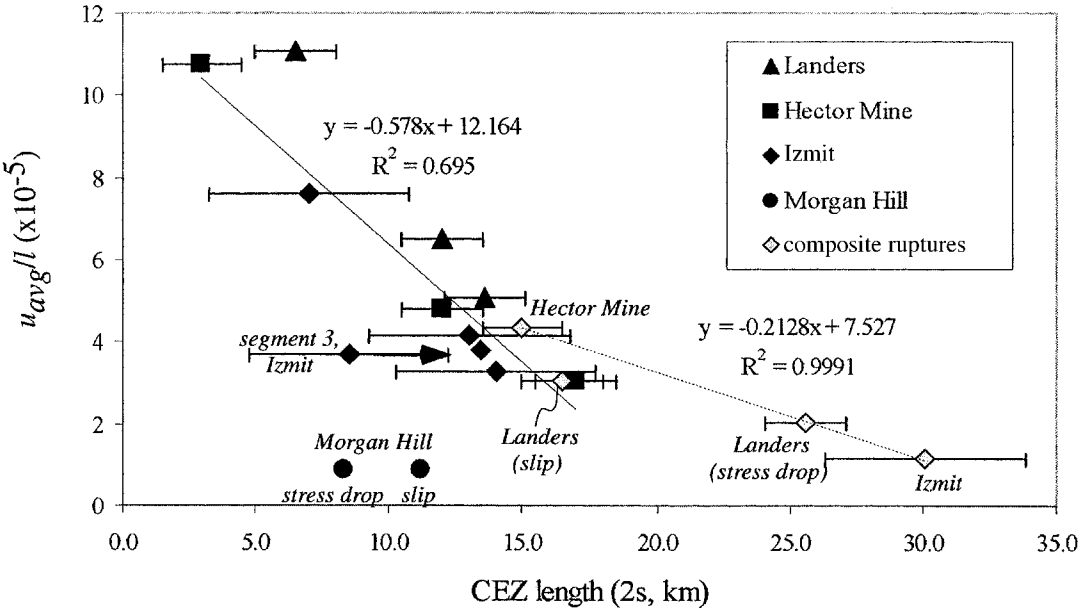

Figure 10. Slip/length (u_{avg}/l) is negatively correlated with measured CEZ lengths ($2s$) for individual segments (filled symbols) and composite ruptures (open diamonds). Error estimates are determined from the resolution of the inversions (Table 3). Rupture parameters for the Morgan Hill earthquake are not included in either fit, and only the parameters determined from the stress drop distribution of Landers are used in the fit to the composite ruptures. Two points are shown for segment 3 of İzmit, and the linear fit shown includes the smaller CEZ length (see text for discussion). The fit to the individual segments is preferred over the fit to the composite ruptures despite the better fit for the latter (see text for details).

strike dimensions (s/a). These error estimates represent the spatial resolution of the 2D slip inversions; for example, the spatial resolution for Hector Mine and Landers is 3.0 km along-strike, or an error ($\pm$) of 1.5 km, which correlates to $\pm \sim 5\%$ of s/a for these rupture segments. We also display an arbitrary error of 20% in average slip (for visualization purposes only), which shows no significant effects.

For the four earthquakes we investigate in this article, the estimates of shear driving stress or shear yield are comparable in magnitude, from ~10 to 25 MPa, despite the range in possible errors. The mean driving stress is ~13 MPa, whereas the mean shear yield strength is ~22 MPa. The estimates from the İzmit segments are lower for both parameters relative to the California earthquakes. The values for the Landers and Hector Mine event are quite similar (Table 3), as expected for these proximal faults occurring within similar rock types and tectonic regime (Mojave Desert, southern California). Calculations based on the composite ruptures yielded values of shear driving stress approximately equivalent to shear yield strength, which is a violation of the model (see Chell, 1977; S&F), and results from unphysically large CEZs for the measured rupture aspect ratio. This is why we prefer the relation between u_{avg}/l and $2s$ for individual rupture segments rather than the composite rupture.

Discussion

Effects of Heterogeneous Slip, Strength, and Stress

The CEZ model presented herein (and more completely by S&F) represents a static solution for brittle failure of a fully bounded rupture patch. The frictional strength of the fault is a fundamental parameter in a CEZ model, with τ_y comparable to the shear strength of the fault surface in the CEZ, and τ_i represented by the depth-averaged shear stress resolved along the fault, associated with an average coefficient of initial sliding friction (μ_i), effective normal stress ($\sigma_n - p_p$), and cohesion ($\tau_i = c_o + \mu_i[\sigma_n - p_p]$). We assume that driving stresses do not vary significantly along the length of plate boundary faults, as expected if slip rates, material properties, and fault orientations are relatively uniform along the length of the boundary. We do not incorporate variations in initial stress, frictional strength, or frictional behavior (besides for the CEZ relative to the remainder of the rupture) that likely occurs with depth throughout the seismogenic thickness of the crust. These variations have been used as a basis for modeling the depth distribution of seismicity (e.g., Sibson, 1982; Tse and Rice, 1986; Marone and Scholz, 1988; Chester, 1995; Marone, 1998; Scholz, 1998). For example, the reduced strength of crustal rock and the existence of a partially bounded rupture requires a re-

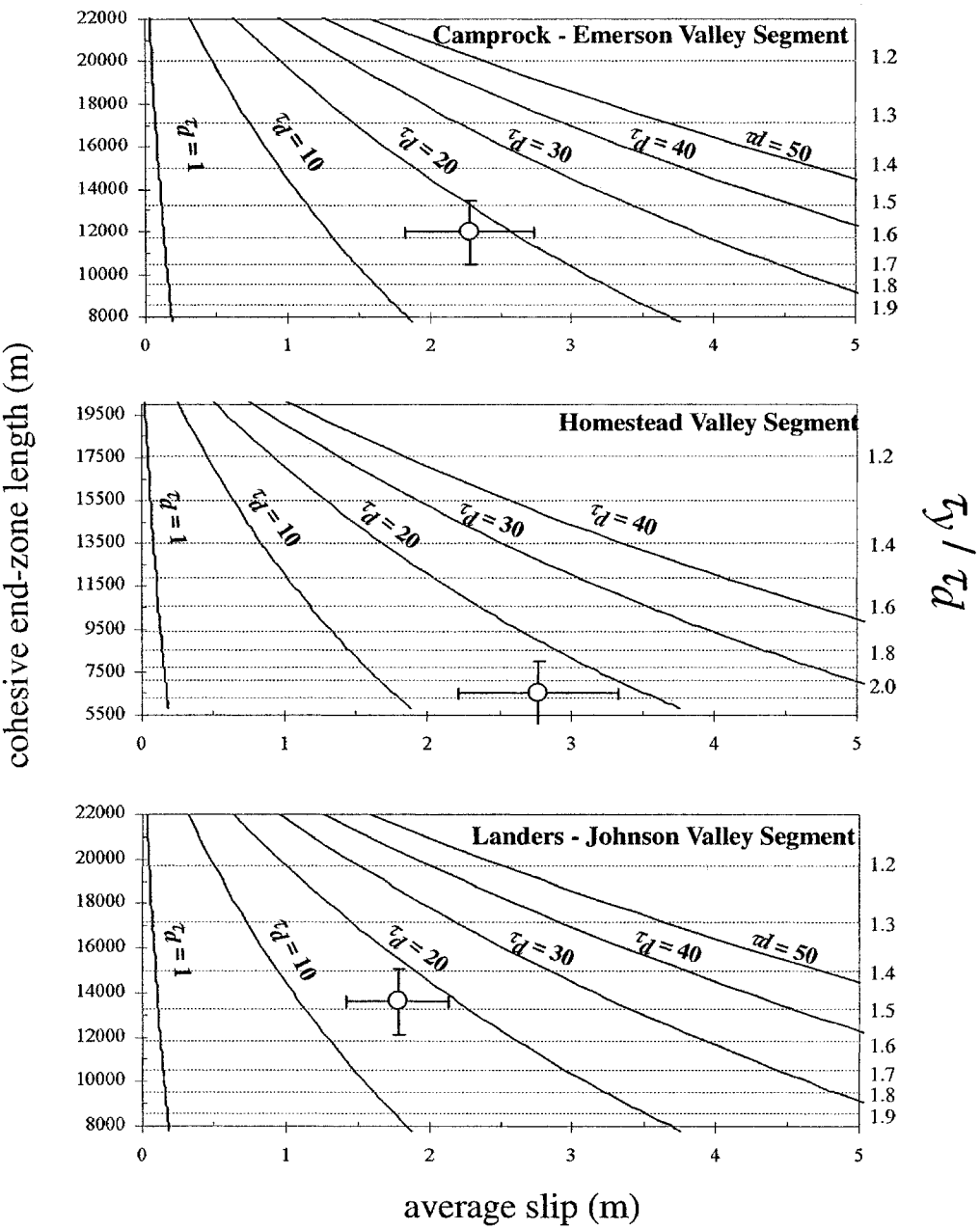

Figure 11. Relations between CEZ lengths, average slip, shear driving stress (τ_y), and ratio of shear yield strength to shear driving stress (τ_y/τ_d) for the 1992 Landers earthquake rupture segments. Error estimates in CEZ lengths are determined from the resolution of the inversions (Table 3), and $\pm 20\%$ in average slip is displayed for visualization purposes. Notice that these error estimates have little effect on the calculated shear driving stress.

duction of τ_y in the near-surface region. This would increase the end zone size in the dip direction (Chell, 1977) and would reduce the average slip. Free-surface effects are likely to be more significant for events with smaller rupture areas and average stress drops (e.g., the 1984 Morgan Hill earthquake) because the end-zone area is then a greater percentage of the total rupture area. However, many coseismic slip distributions exhibit the opposite behavior; higher magnitudes of slip occur near the surface (Figs. 6, 8, and 9). Delouis *et al.* (2002) suggest that the resolution of slip degenerates with depth when inverted for using GPS, InSAR, and strong-motion data, whereas teleseismic data help constrain slip in the deepest portions. Despite this, some physical mechanisms may explain these slip distributions. Such slip

patterns have been attributed to the interplay between postseismic and coseismic slip via stress triggering (Pollitz *et al.*, 1998; Reilinger *et al.*, 2000), and are probably related to the existence of a ductile region below the seismogenic portion of the crust where elastic strain energy does not accumulate (e.g., Marone and Scholz, 1988). Similar mechanisms (aseismic slip) may be responsible for reducing slip along most of the Morgan Hill rupture. Furthermore, the free surface effect is probably not important for the Morgan Hill event where the upper rupture tip was at a depth of ~2.5 km (Beroza and Spudich, 1988; Beroza and Mikumo, 1996). Alternatively, Lin and Parmentier (1988) and Kattenhorn and Pollard (1999) suggested that an increase in lithostatic load with depth, with constant tectonic shear stress, is responsible for increasing the frictional resistance to slip at greater depths (but above the brittle-ductile transition) and results in larger magnitudes of slip (and stress drop) within shallower portions of the crust. Although their results are based on normal faults within extensional regimes, the same arguments (based on Mohr–Coulomb failure) apply in a strike-slip tectonic regime (Kattenhorn, personal comm., 2002). Nevertheless, because material properties are likely to vary more with depth than along strike, and furthermore, because the relative resolution of the down-dip direction (grid spacing in inversion models divided by the down-dip width) is significantly less than the along-strike direction, we did not consider the data robust enough to analyze.

Mechanical interaction between adjacent fault tips at segment boundaries modifies the stress state in these regions (Aydin and Schultz, 1990; Gupta and Scholz, 2000). Consequently, fault segmentation has been observed to play an important role in controlling cumulative slip distributions in both the along-strike (e.g., Peacock, 1991; Dawers and Anders, 1995) and down-dip dimensions (Wilkins and Gross, 2002), as well as the coseismic slip distributions and rupture velocities (Wald and Heaton, 1994; Olsen *et al.*, 1997; Peyrat *et al.*, 2001; Ji *et al.*, 2002; Delouis *et al.*, 2002). Stress interactions may be large enough to restrict propagation (Aydin and Schultz, 1990; Bürgmann *et al.*, 1994; Gupta and Scholz, 2000; Wilkins and Gross, 2002), and furthermore, the CEZ length varies as a function of the degree of restriction to propagation (Wilkins and Gross, 2002). These effects of stress interaction associated with fault segmentation are not accounted for explicitly in our model, although the CEZs were measured from distinct rupture segments, most of which undoubtedly experience mechanical interaction with adjacent rupture segments. The Hector Mine and Landers earthquakes each consist of three rupture segments, İzmit has four, and Morgan Hill has one. Except for Morgan Hill, each slip distribution exhibits multiple peaks and troughs of slip whose spatial variability correlates with each rupture segment and the expected location of CEZs at the rupture segment boundaries. Future modeling work should incorporate the effects of mechanical interaction among segments on initial stress boundary conditions for numerical models of slip.

Stress Magnitudes

In the 3D CEZ rupture model presented herein, the coseismic source parameters are a function of (1) material properties of the surrounding elastic medium, (2) fault shape, (3) peak shear strength in the end zone (τ_y), and (4) the resolved shear stresses (τ_i). The first two parameters are relatively well known, whereas the peak strength and resolved shear stresses cannot be measured from seismic data. CEZ peak shear strengths required by our models to fit the measured slip parameters for the Hector Mine, İzmit, Landers, and Morgan Hill earthquakes, range from ~10 to 30 MPa (Table 3). The shear strengths are roughly twice that required in dynamic simulation of the 1992 Landers earthquake (Olsen *et al.*, 1997; Peyrat *et al.*, 2001), although complete stress drops are assumed and Peyrat *et al.* (2001) note that the absolute magnitude of stress is not constrained by dynamic inversions, just the stress drop. Olsen *et al.* (1997) and Peyrat *et al.* (2001) modulated the ambient stress along the fault unti the slip-weakening friction model they used could reproduce the observed slip distribution determined by Wald and Heaton (1994). Although their model requires yield strengths on the order of 12 MPa, their initial values of shear stress were about half the yield strength, 5 MPa plus or minus that required to reproduce the slip.

The resolved shear stresses required by our model to match the observations are similar to the shear yield strengths (~10–30 MPa), although for each individual segment τ_y/τ_d is an average of ~2. Initial stresses in our models and are thus significantly less than estimates based on Anderson–Byerlee mechanics (100–160 MPa; Scholz, 2000). However, our estimated values of initial shear stress are broadly consistent with values inferred from breakouts and hydrofracture experiments within the Cajon Pass borehole (Zoback and Healy, 1992) and from borehole breakouts and drilling-induced tensile fractures in the SAFOD pilot hole (Hickman and Zoback, 2004). For example, Zoback and Healy (1992) reported maximum and minimum horizontal stress (σH and σh, respectively) gradients of ~35 and ~14.3 MPa/km at Cajon Pass (their figure 6). Taking an average stress (at a depth of 7.5 km) from a linear extrapolation to 15 km results in a $\sigma H \approx 262.5$ MPa and $\sigma h \approx 107$, which implies a maximum shear stress of 77.7 MPa ($\tau_{\max} = (\sigma H - \sigma h)/2$). This value decreases as the angle between σH and the fault normal decreases following $\tau = [(\sigma H - \sigma h)/2] * \sin(2\theta)$, where θ is the angle between σH and the fault normal for a strike-slip fault (e.g., $\tau = 26$ MPa for $\theta = 10°$). The available data support high magnitudes of shear stress in the crust adjacent to strike-slip faults like the San Andreas fault (Zoback and Healy, 1992; Scholz, 2000), although the near fault normal σH (within ~10° as summarized by Zoback and Healy, 1992) implies small magnitudes of resolved shear stress. Data from the SAFOD scientific borehole, drilled to 2.2 km depth at 1.8 km away from the surface trace of the San Andreas fault at Parkfield, California (Hickman and Zoback, 2004), also support small magnitudes

of shear stress (i.e., weak fault in strong crust). These results are not consistent with the strong fault view, such as that recently proposed by Scholz (2000), but are more in line with the lack of frictional heat anomalies in the region (Williams *et al.*, 2004). Hickman and Zoback (2004) calculated $\sigma H \approx 113 \pm 14$ MPa and $\sigma h \approx 49 \pm 9$ MPa at a depth of 1671 m, which corresponds to τ_{max} of ~32 MPa. Borehole breakouts in the pilot hole suggest that σH is oriented $50° \pm 17°$ to the SAF, corresponding to a $\theta = 40° \pm 17°$, and thus a resolved shear stress close to the maximum shear stress (at $\theta = 45°$). Small changes in θ ($\pm 17°$) will reduce the resolved shear stress to 23 ($\theta = 23°$) or 29 ($\theta = 57°$) MPa.

Modeled effective stress drops range from ~0.5 to 3.2 MPa (Table 3) and represent an average over each rupture segment. The high yield strength estimates (~10–30 MPa) and small stress drops implied by our model support a partial stress drop (Brune, 1976) or a self-healing slip pulse model (Heaton, 1990). These ambient shear stresses imply magnitudes of frictional heat generation that are comparable with inferences made from heat flow data that constrain the crustal-average shear stress to <20 MPa (e.g., Brune *et al.*, 1969; Zoback and Healy, 1992; Scholz, 2000; Hickman and Zoback, 2004).

CEZ Size and f_{max}

Distinct CEZ lengths estimated in this article range from ~0.5 to 14 km (Figs. 6–9) and are consistently larger than those previously estimated from characteristics of high-frequency seismic radiation (0.5–2 km; Papageorgiou and Aki, 1983a,b). Papageorgiou and Aki (1983a,b) used the f_{max} parameter, defined as "the high-frequency band-limitation of the radiated field of earthquakes" by Hanks (1982), to measure the CEZ lengths with the approximate static relation $f_{max} \approx v/d$, where v is rupture velocity and d is the length of the CEZ. Implicit to this and more recent numerical models of dynamic rupture (Fujiwara and Irikura, 1991) is the physical link between f_{max} and the deceleration of the rupture front (Zeng *et al.*, 1993), presumably in response to increased frictional resistance in proximity to the asperity edges. In these studies, the CEZ is thought to represent the region where slip suddenly decreases and is therefore associated with the region of significant curvature in the slip-length curve. This definition of the CEZ is different from the one used in this article, where the CEZ continues from the tail (Fig. 1) or asperity edge, out to the rupture tip where slip reaches zero or an adjacent segment where slip begins to increase again (e.g., Rudnicki, 1980; Cowie and Scholz, 1992; Bürgmann *et al.*, 1994; Cooke, 1997; Martel, 1997; S&F). In this case the CEZ is larger than that required to produce any characteristic high-frequency radiation and is more akin to a barrier interval or a region of small slip (Aki, 1979). Furthermore, considerable debate exists concerning whether f_{max} is related to some fundamental source dimension (CEZs; Papageorgiou and Aki, 1983a,b; Fujiwara and Irikura, 1991) or results from the attenuation of high-frequency radiation near the Earth's surface (Hanks, 1982; Anderson, 1986), although it is probably related in part to both phenomena (Purvance and Anderson, 2003). Regardless of the importance of near-surface attenuation, we suggest that the large CEZs that we estimate and measure are physically different than the CEZs inferred from high-frequency radiation.

Hypocentral Locations and Fault Nucleation

The CEZ model we present here incorporates strength perturbations along the rupture patch prior to slip. Postslip differences in average yield strength between the CEZ and the yielded portion of the rupture likely develop from a combination of processes. We suggest that the difference in dynamic frictional behavior is an important one (Fig. 1), similar to that found in dynamic models of rupture for the Landers (Olsen *et al.*, 1997; Peyrat *et al.*, 2001) and Morgan Hill (Mikumo and Miyatake, 1995; Beroza and Mikumo, 1996) earthquakes and inferred from an interpretation of the İzmit earthquake (Reilinger *et al.*, 2000). Although interseismic deformation, in the form of either aftershocks or creep, may reduce stress in the CEZ and effectively homogenize the stress along the future rupture surface, we hypothesize that subsequent mainshocks may preferentially nucleate at the tails of former CEZs in response to the differences in frictional behavior. Supportive evidence for this is revealed by the location of hypocenters in each slip distribution we considered.

Curiously, the hypocenters all occur on contours of slip that spatially correspond to the tail of the CEZ (Table 3 and Figs. 6–9). In a CEZ model, propagation is predicted to initiate once the slip at the tail of the CEZ reaches a large enough value so that τ_y can be reduced to τ_f, or in other words, when the available energy for work in the CEZ is equivalent to the critical value of the energy release rate (G_c) necessary for slip (Palmer and Rice, 1973; Rudnicki, 1980). The correspondence suggests that the CEZ existed prior to the rupture, although this does not preclude a stress increase (and negative stress drop) in the CEZs immediately following rupture as well. This stress feedback may provide clues into long-term behavioral patterns along the fault (e.g., Heimpel, 1997), such as repeating earthquakes (Vidale *et al.*, 1994; Ellsworth, 1995; Rubin *et al.*, 1999). Recent interpretations of heterogeneous slip behavior on currently creeping fault segments, with areas that exhibit stable sliding (i.e., aseismic creep) adjacent to regions experiencing stick-slip behavior (Vidale *et al.*, 1994; Rubin *et al.*, 1999), provide evidence for differences in frictional behavior along a single fault surface prior to a large event. Detailed observations of earthquake locations throughout multiple seismic cycles indicate that earthquakes exhibit quasiperiodic behavior in both the spatial and temporal domains (e.g., Vidale *et al.*, 1994; Ellsworth, 1995; Nadeau and Johnson, 1998). This implies that the process responsible for forming a CEZ may repeatedly occur at the same location through multiple seismic cycles.

We suggest that the region of increased frictional resistance (CEZ) is associated with regions that may have similar values of static friction but which experience differences in dynamic behavior (Heaton, 1990), such as slip strengthening (e.g., Marone, 1998; Scholz, 1998). However, it is unclear why these dynamic differences in frictional behavior would cause hypocenters to nucleate preferentially at the CEZ tail, especially if initial static friction was similar in the CEZ and the rest of the rupture surface. Perhaps aseismic slip within the CEZ causes stress perturbations at its boundary, which eventually become large enough to nucleate slip on adjacent locked portions of the fault. Reilinger *et al.* (2000) discuss a similar scenario for the İzmit earthquake: slip initiated on a portion of the fault that experienced aseismic slip prior to the coseismic event, and furthermore, afterslip (i.e., creep) is concentrated in regions that experienced relatively small slip during the coseismic phase, including the hypocentral, shallow, and deepest portions of the fault. More sophisticated techniques may be required to locate simultaneously the hypocenter and determine the magnitude of slip in the hypocentral region, possibly by inverting a combination of strong motion and geodetic data for a variety of hypocentral depths to determine the best-fit solution (e.g., Ji *et al.*, 2002), together with the double-difference technique of earthquake location (Waldhauser and Ellsworth, 2000). Accurate determination of these parameters and increased resolution of the inversion models, combined with observations from numerous earthquakes (not necessarily strike-slip), would provide a better understanding of the importance of CEZs in the nucleation of seismic slip.

Conclusions

A new fracture mechanics model of coseismic slip with elliptical rupture geometries and CEZs is consistent with the general scaling relations of slip and rupture aspect ratio for continental, interplate strike-slip faults. However, significant variability in the data indicate that fitting all earthquake observations with a single curve, at least in the form of average slip versus rupture length or aspect ratio, is not possible. In terms of a CEZ model, this implies a difference in the ratio of yield shear strength (τ_y) to driving shear stress (τ_d) for individual earthquakes of similar sizes, which in turn is controlled by variations in end-zone size and stress drop. We interpret cohesive end-zone lengths from 2D distributions of stress drop and slip determined from joint inversions of seismic and geodetic data to test the hypothesis that differences in CEZ dimensions are responsible for these variations. The correspondence among observed source parameters and effects of the CEZ offers a physically based solution to the long-standing debate in seismology concerning the scaling of continental, interplate strike-slip earthquakes, in that the scaling of these events is controlled by rupture dimensions *and* CEZ lengths. This refined model, which is similar to that proposed by Mai and Beroza (2000), provides additional degrees of freedom compared with end-member *L* and *W* models, as well as a physically based reason for the intrinsic variability in stress drops for earthquakes of similar rupture dimensions.

The equations for stress drop associated with our new model are an improvement to conventional formulae that are inconsistent with observed scaling behavior. This new equation for stress drop offers the significant advantage of estimating the required magnitude of absolute shear stress resolved along the rupture. A comparison of source parameters with this model suggests that resolved shear stresses are 10–30 MPa, but stress drops are low (<3 MPa), supporting a partial stress drop model of earthquake rupture. Because this model has important implications for the energy budget during coseismic rupture, it should be tested with additional earthquakes whose spatial distributions of slip are well determined. Furthermore, the agreement between predicted locations of rupture nucleation at certain magnitudes of slip in our model is encouraging and indicates that additional efforts should focus on this class of rupture models.

A major improvement to this analysis may be achieved if slip behaviors and fault geometries along the rupture surface, determined prior to rupture, could be compared with the coseismic slip and stress drop distributions to calibrate and verify specifics of the CEZ model. Such an analysis would provide the critical link between known fault properties, expected slip, and stress drop, and eventually may lead to a prediction of strong-motion characteristics associated with a major rupture. New techniques of locating earthquakes (e.g., Waldhauser and Ellsworth, 2000) that have led to the identification and mapping of characteristic slip behaviors, such as locked regions that produce repeating earthquakes and other areas that exhibit stable slip (Vidale *et al.*, 1994; Rubin *et al.*, 1999), provide promising avenues for our predictive capabilities of seismicity when linked with physical models such as the one used in this article.

Acknowledgments

Funding for this project was provided by grants from NASA's Planetary Geology and Geophysics and Mars Data Analysis Programs to R.A.S. S. W. is grateful to D. Wald, G. Beroza, B. Delouis, and S. Peyrat for providing slip and stress drop distribution data, and Y. Zeng, J. G. Anderson, R. Schweickert, M. Purvance, and J. N. Brune for discussions and comments on an earlier draft. BSSA reviewers P. Martin Mai, Bruce E. Shaw, and David D. Oglesby are thanked for their thoughtful reviews.

References

Abercrombie, R. E. (1995). Earthquake source scaling relationships from −1 to 5 M_L using seismograms recorded at 2.5 km depth, *J. Geophys. Res.* **100,** 24,015–24,036.

Aki, K. (1979). Characterization of barriers on an earthquake fault, *J. Geophys. Res.* **84,** 6140–6148.

Akyuz, E., A. Barka, E. Altunel, R. Hartleb, and G. Sunal (2000). Observations and slip distribution of the November 12, 1999 Duzce earthquake (M = 7.1), Bolu, Turkey, in *The 1999 İzmit and Duzce Earthquakes: Preliminary Results*, A. Barka, O. Kozaci, S. Akyuz, and E. Altunel (Editors), Istanbul Technical University, 15–30.

Anderson, J. G. (1986). Implication of attenuation for studies of the earthquake source, in *Earthquake Source Mechanics*, S. Das, J. Boatwright, and C. H. Scholz (Editors), American Geophysical Union Monograph **37,** 297–309.

Aydin, A., and R. A. Schultz (1990). Effect of mechanical interaction on the development of strike-slip faults with échelon patterns, *J. Struct. Geol.* **12,** 123–129.

Barenblatt, G. I. (1962). The mathematical theory of equilibrium cracks in brittle fracture, *Adv. Appl. Mech.* **7,** 55–125.

Barka, A., H. S. Akyüz, E. Altunel, G. Sunal, Z. Çakir, A. Dikbas, B. Yerli, R. Armijo, B. Meyer, J. B. de Chabalier, T. Rockwell, J. R. Dolan, R. Hartleb, T. Dawson, S. Christofferson, A. Tucker, T. Fumal, R. Langridge, H. Stenner, W. Lettis, J. Bachhuber, and W. Page (2002). The surface rupture and slip distribution of the 17 August 1999 İzmit earthquake (M 7.4), North Anatolian fault, *Bull. Seism. Soc. Am.* **92,** 43–60.

Beeler, N., D. L. Lockner, and S. H. Hickman (2001). A simple stick-slip and creep slip model for repeating earthquakes and its implications for microearthquakes at Parkfield, *Bull. Seism. Soc. Am.* **91,** 1797–1804.

Bell, J. W., C. M. dePolo, A. R. Ramelli, A. M. Sarna-Wojcicki, and C. E. Meyer (1999). Surface faulting and paleoseismic history of the 1932 Cedar Mountain earthquake area, west-central Nevada, and implications for modern tectonics of the Walker Lane, *Geol. Soc. Am. Bull.* **111,** 791–807.

Beroza, G. C., and T. Mikumo (1996). Short slip duration in dynamic rupture in the presence of heterogeneous fault properties, *J. Geophys. Res.* **101,** 22,449–22,460.

Beroza, G. C., and P. Spudich (1988). Linearized inversion for fault rupture behavior; application to the 1984 Morgan Hill, California, earthquake, *J. Geophys. Res.* **93,** 6275–6296.

Biegel, R. L., and C. G. Sammis (1989). The frictional properties of a simulated gouge having a fractal particle distribution, *J. Struct. Geol.* **11,** 827–846.

Blanpied, M. L., D. A. Lockner, and J. D. Byerlee (1995). Frictional slip of granite at hydrothermal conditions, *J. Geophys. Res.* **100,** 13,045–13,064.

Bodin, P., and J. N. Brune (1996). On the scaling of slip with rupture legth for shallow strike-slip earthquakes: quasi-static models and dynamic rupture propagation, *Bull. Seism. Soc. Am.* **86,** 1292–1299.

Brune, J. N. (1976). The physics of earthquake strong motion, in *Seismic Risk and Engineering Decisions*, and C. Lomnitz and E. Rosenblueth (Editors), Elsevier, New York, 140–177.

Brune, J. N., T. L. Henyey, and R. F. Roy (1969). Heat flow, stress, and rate of slip along the San Andreas fault, California, *J. Geophys. Res.* **74,** 3821–3827.

Bürgmann, R., D. D. Pollard, and S. J. Martel (1994). Slip distributions on faults: effects of stress gradients, inelastic deformation, heterogeneous host-rock stiffness, and fault interaction, *J. Struct. Geol.* **16,** 1675–1690.

Byerlee, J. D. (1967). Theory of friction based on brittle fracture, *J. Appl. Phys.* **38,** 2928–2934.

Chell, G. G. (1977). The application of post-yield fracture mechanics to penny-shaped and semi-circular cracks, *Eng. Fract. Mech.* **9,** 55–63.

Chester, F. M. (1995). A rheologic model for wet crust applied to strike-slip faults, *J. Geophys. Res.* **100,** 13,033–13,044.

Cooke, M. L. (1997). Fracture localization along faults with spatially varying friction, *J. Geophys. Res.* **102,** 22,425–22,434.

Cowie, P. A., and C. H. Scholz (1992). Physical explanation for the displacement-length relationship of faults using a post-yield fracture mechanics model, *J. Struct. Geol.* **14,** 1133–1148.

Cowie, P. A., and Z. K. Shipton (1998). Fault tip displacement gradients and process zone dimensions, *J. Struct. Geol.* **20,** 983–997.

Dawers, N. H., and M. H. Anders (1995). Displacement-length scaling and fault linkage, *J. Struct. Geol.* **14,** 607–614.

Delouis, B., P. Lundgren, J. Salichon, and D. Giardini (2002). Joint inversion of InSAR, GPS, teleseismic, and strong-motion data for the spatial and temporal distribution of earthquake slip: application to the 1999 İzmit (Turkey), earthquake, *Bull. Seism. Soc. Am.* **92,** 278–299.

Dugdale, D. S. (1960). Yielding of steel sheets containing slits, *J. Mech. Phys. Solids* **8,** 100–104.

Ellsworth, W. L. (1995). Characteristic earthquakes and long-term earthquake hazard forecasts: Implications of Central California Seismicity, in *Urban Disaster Mitigation: The Role of Science and Technology*, F. Y. Cheng and and M. S. Sheu (Editors), Elsevier Science Ltd., New York, 1–14.

Eshelby, J. D. (1957). The determination of the elastic field of an ellipsoidal inclusion, and related problems, *Proc. R. Soc. London A* **241,** 376–396.

Fujiwara, H., and K. Irikura (1991). High-frequency seismic-wave radiation from antiplane cohesive zone model and f_{max} as source effect, *Bull. Seism. Soc. Am.* **3,** 1115–1128.

Galehouse, J. S., and J. J. Lienkaemper (2003). Inferences drawn from two decades of alinement array measurements of creep on faults in the San Francisco Bay region, *Bull. Seism. Soc. Am.* **93,** 2415–2433.

Gu, Y., and T.-F. Wong (1994). Development of shear localization in simulated quartz gouge: effects of cumulative slip and gouge particle size, *Pure Appl. Geophys.* **143,** 387–423.

Gupta, A., and C. H. Scholz (2000). A model of normal fault interaction based on observations and theory, *J. Struct. Geol.* **22,** 865–879.

Hanks, T. C. (1977). Earthquake stress drops, ambient tectonic stresses, and stresses that drive plates, *Pure Appl. Geophys.* **115,** 441–458.

Hanks, T. C. (1982). f_{max}, *Bull. Seism. Soc. Am.* **72,** 1867–1880.

Heaton, T. (1990). Evidence for and implications of self-healing pulses of slip in earthquake rupture, *Phys. Earth Planet. Interiors* **64,** 1–20.

Heimpel, M. (1997). Critical behavior and the evolution of fault strength during earthquake cycles, *Nature* **388,** 865–868.

Hickman, S., and M. D. Zoback (2004). Stress orientations and magnitudes in the SAFOD pilot hole, *Geophys. Res. Lett.* **31,** L15S12, doi 10.1029/2004GL020043.

Ingraffea, A. R. (1987). Theory of crack initiation and propagation in rock, in *Fracture Mechanics of Rock*, B. K. Atkinson (Editor), Academic Press, London, 71–110.

Ji, C., D. J. Wald, and D. V. Helmberger (2002). Source description of the 1999 Hector Mine, California earthquake, part II: complexity of slip history, *Bull. Seism. Soc. Am.* **92,** 1073–1095.

Kanamori, H., and D. L. Anderson (1975). Theoretical basis of some empirical relations in seismology, *Bull. Seism. Soc. Am.* **65,** 1073–1095.

Kattenhorn, S. A., and D. D. Pollard (1999). Is lithostatic loading important for the slip behavior and evolution of normal faults in the Earth's crust? *J. Geophys. Res.* **104,** 28,879–28,898.

Kelson, K. I., J. Tohurst, and D. Manaker (1999). Earthquakes on the Calaveras fault: fact or fiction? The geology, seismology, and paleoseismology of the Calaveras fault, in *Geologic Field Tips in Northern California, Calif. Div. Mines Geol. Spec. Rept. 119*, 160–175.

Knopoff, L. (1958). Energy release in earthquakes, *Geophys. J.* **1,** 44–52.

Lawn, B. R. (1993). *Fracture of Brittle Solids*, 2nd Ed. Cambridge University Press, New York.

Lee, Y., J. G. Anderson, and Y. Zeng (2000). Evaluation of empirical ground-motion relations in southern California, *Bull. Seism. Soc. Am.* **90,** 136–148.

Li, V. C. (1987). Mechanics of shear rupture applied to earthquake zones, in *Fracture Mechanics of Rock*, B. K. Atkinson (Editor), Academic Press, London, 351–428.

Lin, A., B. Fu, J. Guo, Q. Zeng., G. Dang, W. He, and Y. Zhao (2002). Co-seismic strike-slip and rupture length produced by the 2001 Ms 8.1 Central Kunlun earthquake, *Science* **296,** 2015–2017.

Lin, J., and E. M. Parmentier (1988). Quasistatic propagation of a normal fault: a fracture mechanics model, *J. Struct. Geol.* **10,** 249–262.

Maggi, A., J. A. Jackson, D. McKenzie, and K. Priestley (2000). Earthquake focal depths, effective elastic thickness, and the strength of the continental lithosphere, *Geology* **28,** 495–498.

Mai, P. M., and G. C. Beroza (2000). Source scaling properties from finite-fault-rupture models, *Bull. Seism. Soc. Am.* **90,** 604–615.

Marone, C. (1998). Laboratory-derived friction laws and their application to seismic faulting, *Annu. Rev. Earth Planet. Sci.* **26,** 643–696.

Marone, C., C. B. Raleigh, and C. H. Scholz (1990). Frictional behavior and constitutive modeling of simulated fault gouge, *J. Geophys. Res.* **95,** 7007–7025.

Marone, C., and C. H. Scholz (1988). The depth of seismic faulting and the upper transition from stable to unstable slip regimes, *Geophys. Res. Lett.* **15,** 621–624.

Martel, S. J. (1997). Effects of cohesive zones on small faults and implications for secondary fracturing and fault trace geometry, *J. Struct. Geol.* **19,** 835–847.

Martel, S. J., and W. A. Boger (1998). Geometry and mechanics of secondary fracturing around small three-dimensional faults in granitic rock, *J. Geophys. Res.* **103,** 21,299–21,314.

Martel, S. J., and D. D. Pollard (1989). Mechanics of slip and fracture along small faults and simple strikeslip fault zones in granitic rock, *J. Geophys. Res.* **94,** 9417–9428.

Mikumo, T., and T. Miyatake (1995). Heterogeneous distribution of dynamic stress drop and relative fault strength recovered from the results of waveform inversion: the 1984 Morgan Hill, California, earthquake, *Bull. Seism. Soc. Am.* **85,** 178–193.

Miller, S. A. (2002a). Earthquake scaling and the strength of seismogenic faults *Geophys. Res. Lett.* **29,** 2002, doi 10.1029/2001GL014181.

Miller, S. A. (2002b). Properties of large ruptures and the dynamical influence of fluids on earthquakes and faulting, *J. Geophys. Res.* **107,** 2002, doi 10.1029/2000JB000032.

Nadeau, R. M., and L. R. Johnson (1998). Seismological studies at Parkfield VI: moment release rates and estimates of source parameters for small repeating earthquakes, *Bull. Seism. Soc. Am.* **88,** 790–814.

Okubo, P. G., and J. H. Dieterich (1984). Effects of fault properties on frictional instabilities produced on simulated faults, *J. Geophys. Res.* **89,** 5817–5827.

Olsen, K. B., R. Madariaga, and R. J. Archuleta (1997). Three-dimensional dynamic simulation of the 1992 Landers Earthquake, *Science* **278,** 834–838.

Palmer, A. C., and J. R. Rice (1973). The growth of slip surfaces in the progressive failure of over-consolidated clay. *Proc. R. Soc. London A* **332,** 527–548.

Papageorgiou, A. S., and K. Aki (1983a). A specific barrier model for the quantitative description of inhomogeneous faulting and the prediction of strong ground motion, part I: description of the model, *Bull. Seism. Soc. Am.* **73,** 693–722.

Papageorgiou, A. S., and K. Aki (1983b). A specific barrier model for the quantitative description of inhomogeneous faulting and the prediction of strong ground motion, part II: applications of the model, *Bull. Seism. Soc. Am.* **73,** 953–978.

Peacock, D. C. P. (1991). Displacement and segment linkage in strike-slip fault zones, *J. Struct. Geol.* **13,** 1025–1035.

Peyrat, S., K. Olsen, and R. Madariaga (2001). Dynamic modeling of the 1992 Landers earthquake, *J. Geophys. Res.* **106,** 26,467–26,482, 2001, doi 10.1029/2001JB000205.

Pollard, D. D., and P. Segall (1987). Theoretical displacements and stresses near fractures in rock: with applications to faults, joints, veins, dikes, and solution surfaces, in *Fracture Mechanics of Rock*, B. K. Atkinson (Editor), Academic Press, London, 277–349.

Pollitz, F., R. Bürgmann, and P. Segall (1998). Joint estimation of afterslip rate and postseismic relaxation following the 1989 Loma Prieta earthquake, *J. Geophys. Res.* **103,** 26,975–26,992.

Prejean, S. G., and W. L. Ellsworth (2001). Observations of earthquake source parameters at 2 km depth in the Long Valley Caldera, Eastern California, *Bull. Seism. Soc. Am.* **91,** 165–177.

Purvance, M. D., and J. G. Anderson (2003). A comprehensive study of the observed spectral decay in strong motion accelerations recorded in Guerrero, Mexico, *Bull. Seism. Soc. Am.* **93,** 600–611.

Reilinger, R. E., S. Ergintav, R. Bürgmann, S. McClusky, O. Lenk, A. Barka, O. Gurkan, L. Hearn, K. L. Feigl, R. Cakmak, B. Aktug, H. Ozener, and M. N. Toksoz (2000). Coseismic and postseismic fault slip for the 17 August 1999, M = 7.5, İzmit, Turkey earthquake, *Science* **289,** 1519–1524.

Romanowicz, B. (1992). Strike-slip earthquakes on quasi-vertical transcurrent faults: inferences for general scaling relations, *Geophys. Res. Lett.* **19,** 481–484.

Romanowicz, B. (1994). A reappraisal of large earthquake scaling; discussion and reply, *Bull. Seism. Soc. Am.* **84,** 1675–1678.

Rubin, A. M. (1993) Tensile fracture of rock at high confining pressure: implications for dike propagation, *J. Geophys. Res.* **98,** 15,919–15,935.

Rubin, A. M., D. Gillard, and J.-L. Got (1999). Streaks of microearthquakes along creeping faults, *Nature* **400,** 635–641.

Rudnicki, J. W. (1980). Fracture mechanics applied to the earth's crust, *Annu. Rev. Earth Planet. Sci.* **8,** 489–525.

Schell, M. M., and L. J. Ruff (1989). Rupture of a seismic gap in southeastern Alaska: the Sitka earthquake (Ms 7.6), *Phys. Earth Planet. Interiors* **54,** 241–257.

Scholz, C. H. (1982). Scaling laws for large earthquake: consequences for physical models, *Bull. Seism. Soc. Am.* **72,** 1–14.

Scholz, C. H. (1990). *The Mechanics of Earthquakes and Faulting*, Cambridge University Press, New York, 439 pp.

Scholz, C. H. (1994a). A reappraisal of large earthquake scaling, *Bull. Seism. Soc. Am.* **84,** 215–218.

Scholz, C. H. (1994b). Reply to comments on "A reappraisal of large earthquake scaling", *Bull. Seism. Soc. Am.* **84,** 1677–1678.

Scholz, C. H. (1998). Earthquakes and friction laws, *Nature* **391,** 37–42.

Scholz, C. H. (2000). Evidence for a strong San Andreas fault, *Geology* **28,** 163–166.

Scholz, C. H., C. A. Aviles, and S. G. Wesnousky (1986). Scaling differences between interplate and intraplate earthquakes, *Bull. Seism. Soc. Am.* **76,** 65–70.

Schultz, R. A., and H. Fossen (2002). Displacement-length scaling in three dimensions: the importance of aspect ratio and application to deformation bands, *J. Struct. Geol.* **24,** 1389–1411.

Scientists from the U.S. Geological Survey (USGS), Southern California Earthquake Center (SCEC), and California Division of Mines and Geology (CDMG) (2000). Preliminary report on the 16 October 1999 M 7.1 Hector Mine, California, earthquake, *Seism. Res. Lett.* **71,** 11–23.

Shaw, B. E., and C. H. Scholz (2001). Slip-length scaling in large earthquakes: observations and theory and implications for earthquake physics, *Geophys. Res. Lett.* **15,** 2995–2998.

Sibson, R. H. (1982). Fault zone models, heat flow, and the depth distribution of earthquakes in the continental crust of the United States, *Bull. Seism. Soc. Am.* **72,** 151–163.

Sieh, K., L. Jones, E. Hauksson, K. Hudnut, D. Eberhart-Phillips, T. Heaton, S. Hough, K. Hutton, H. Kanamori, A. Lilje, S. Lindvall, S. McGill, J. Mori, C. Rubin, J. A. Spotila, J. Stock, H. Thio, J. Treiman, B. Wernicke, and J. Zachariasen (1993). Near-field investigation of the Landers earthquake sequence, April to July, 1992, *Science* **260,** 171–176.

Tibi, R., G. Bock, Y. Xia, M. Baumbach, H. Grosser, C. Milkereit, S. Karakisa, S. Zunbul, R. Kind, and J. Zschau (2000). Rupture processes of the August 17, İzmit and November 12, 1999 Dueze (Turkey) earthquakes, *Geophys. J. Int.* **144,** F1–F7.

Tse, S. T., and J. R. Rice (1986). Crustal earthquake instability in relation to the depth variation in frictional slip properties, *J. Geophys. Res.* **91,** 9452–9472.

Vermilye, J. M., and C. H. Scholz (1998). The process zone; a microstructural view of fault growth, *J. Geophys. Res.* **10,** 12,223–12,237.

Vidale, J. E., W. L. Ellsworth, A. Cole, and C. Marone (1994). Variations in rupture process with recurrence interval in a repeated small earthquake, *Nature* **368,** 624–626.

Wald, D. J., and R. W. Graves (2001). Resolution analysis of finite fault source inversion using one- and three-dimensional Green's functions: part 2, combining seismic and geodetic data, *J. Geophys. Res.* **106,** 8767–8788.

Wald, D. J., and T. H. Heaton (1994). Spatial and temporal distribution of slip for the 1992 Landers, California, earthquake, *Bull. Seism. Soc. Am.* **84,** 668–691.

Waldhauser, F., and W. L. Ellsworth (2000). A double-difference earthquake location algorithm: method and application to the Northern Hayward fault, California, *Bull. Seism. Soc. Am.* **90,** 1353–1368.

Wells, D. L., and K. J. Coppersmith (1994). New empirical relationships among magnitude, rupture length, rupture width, rupture area, and surface displacement, *Bull. Seism. Soc. Am.* **84,** 974–1002.

Wilkins, S. J., and M. R. Gross (2002). Normal fault growth in layered rocks at Split Mountain, Utah: influence of mechanical stratigraphy on dip linkage, fault restriction and fault scaling, *J. Struct. Geol.* **24,** 1413–1429.

Willemse, E. J. M. (1997). Segmented normal faults: correspondence between three-dimensional mechanical models and field data, *J. Geophys. Res.* **102,** 675–692.

Williams, C. F., F. V. Grubb, and S. P. Galanis (2004). Heat flow in the San Andreas Fault Observatory (SAFOD) pilot hole and implications for the strength of the San Andreas fault, *Geophys. Res. Lett.* **31,** L15S14, doi 10.1029/2003GL019352.

Yin, Z.-M., and G. C. Rogers (1996). Toward a physical understanding of earthquake scaling relations, *Pageoph* **146,** 661–675.

Zeng, Y., K. Aki, and T-L. Teng (1993). Mapping of the high-frequency source radiation for the Loma Prieta earthquake, California, *J. Geophys. Res.* **98,** 11,981–11,993.

Zoback, M. D., and J. H. Healy (1992). In situ stress measurements to 3.5 km depth in the Cajon Pass scientific research borehole: implications for the mechanics of crustal faulting, *J. Geophys. Res.* **97,** 5039–5057.

Appendix

Figures A1, A2, and A3 are on following pages.

Geomechanics-Rock Fracture Group
Department of Geological Sciences and Engineering
Mackay School of Earth Sciences and Engineering (172)
University of Nevada
Reno, Nevada 89557-0138

Manuscript received 10 April 2002.

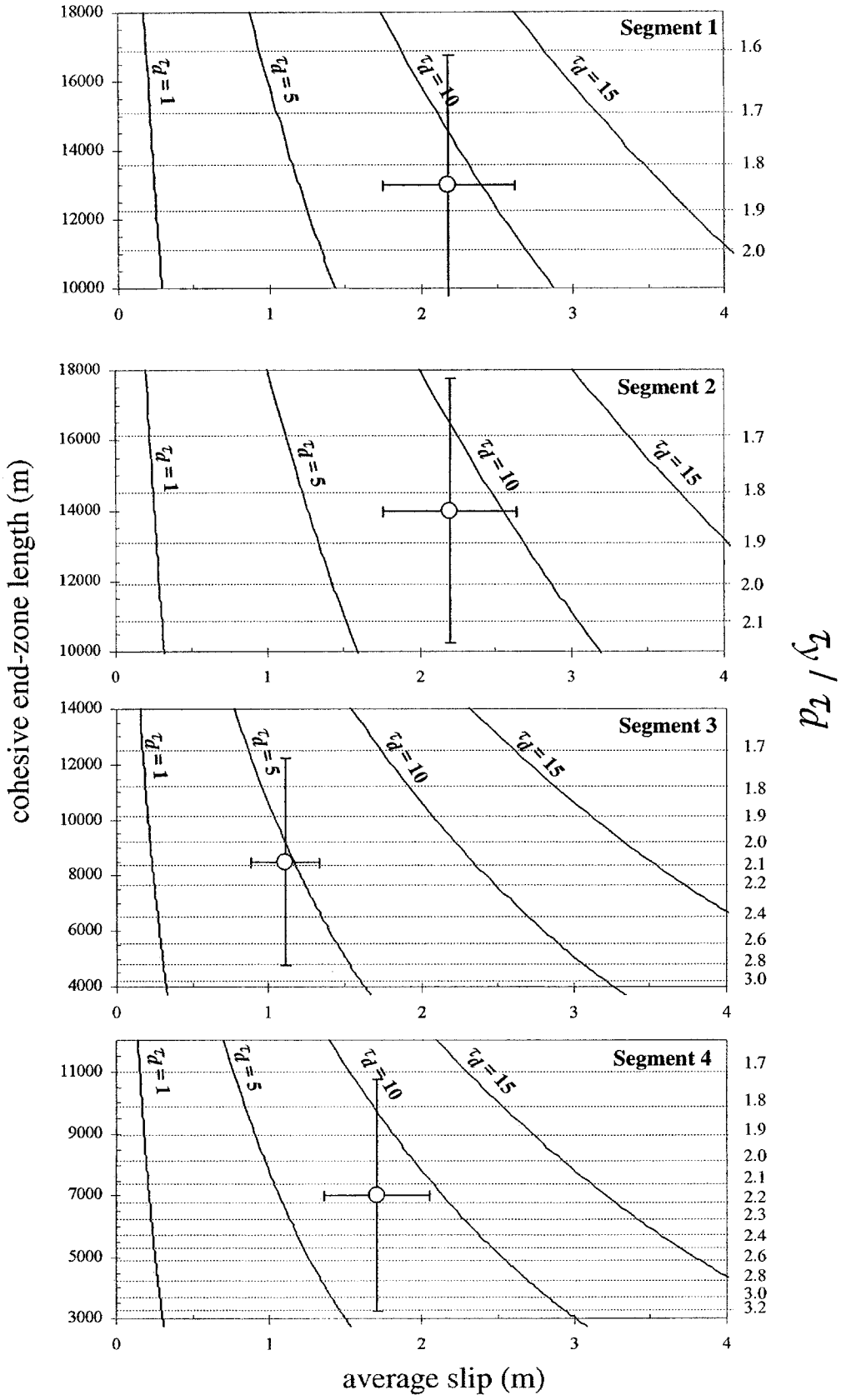

Figure A1. Relations between CEZ lengths, average slip, shear driving stress (τ_y), and ratio of shear yield strength to shear driving stress (τ_y/τ_d) for the 1999 İzmit rupture segments. Error estimates in CEZ lengths are determined from the resolution of the inversions (Table 3), and $\pm 20\%$ in average slip is displayed for visualization purposes.

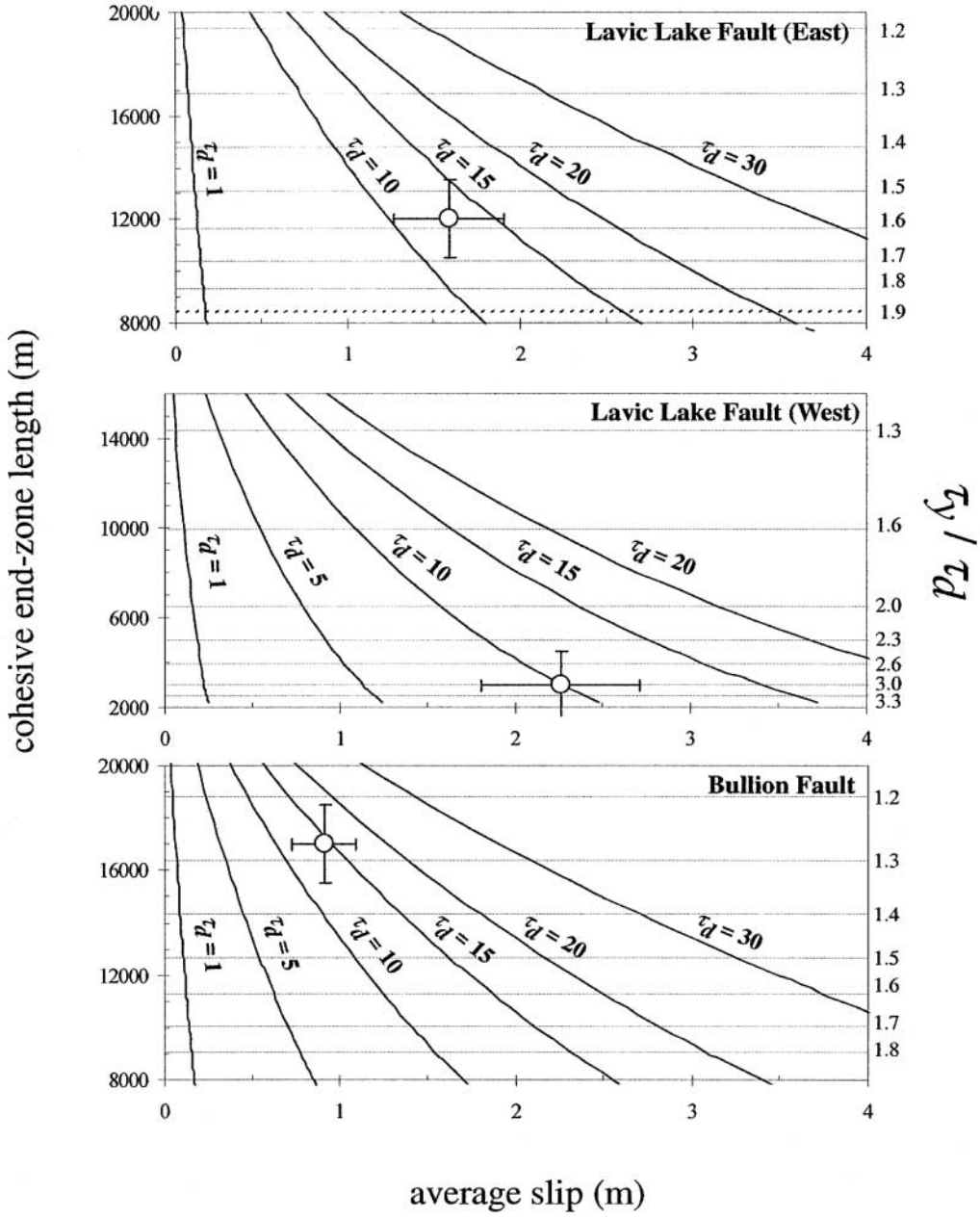

Figure A2. Relations between CEZ lengths, average slip, shear driving stress (τ_y), and ratio of shear yield strength to shear driving stress (τ_y/τ_d) for the 1999 Hector Mine rupture segments. Error estimates in CEZ lengths are determined from the resolution of the inversions (Table 3), and $\pm 20\%$ in average slip is displayed for visualization purposes.

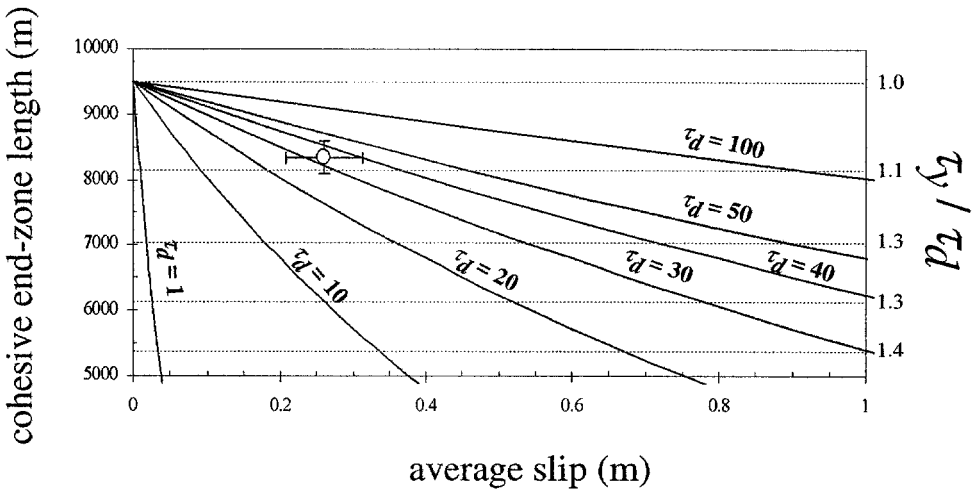

Figure A3. Relations between CEZ lengths, average slip, shear driving stress (τ_y), and ratio of shear yield strength to shear driving stress (τ_y/τ_d) for the 1984 Morgan Hill rupture. Error estimates in CEZ lengths are determined from the resolution of the inversions (Table 3), and $\pm 20\%$ in average slip is displayed.